BACKWARD PRECESSIONAL WHIP AND WHIRL FOR A TWO-POINT RUBBING CONTACT MODEL OF A RIGID ROTOR SUPPORTED BY AN ELASTICALLY SUPPORTED RIGID STATOR

A Thesis

by

DHRUV DILEEP KUMAR

Submitted to the Office of Graduate Studies of
Texas A&M University
in partial fulfillment of the requirements for the degree of

MASTER OF SCIENCE

August 2010

Major Subject: Mechanical Engineering

BACKWARD PRECESSIONAL WHIP AND WHIRL FOR A TWO-POINT RUBBING CONTACT MODEL OF A RIGID ROTOR SUPPORTED BY AN ELASTICALLY SUPPORTED RIGID STATOR

A Thesis

by

DHRUV DILEEP KUMAR

Submitted to the Office of Graduate Studies of
Texas A&M University
in partial fulfillment of the requirements for the degree of

MASTER OF SCIENCE

Approved by:

Chair of Committee,	Dara Childs
Committee Members,	Alan Palazzolo
	James Morgan
Head of Department,	Dennis O' Neal

August 2010

Major Subject: Mechanical Engineering

ABSTRACT

Backward Precessional Whip and Whirl for a Two-Point Rubbing Contact Model of a
Rigid Rotor Supported by an Elastically Supported Rigid Stator.
(August 2010)
Dhruv Dileep Kumar, B.Tech., NIT Kurukshetra, India
Chair of Advisory Committee: Dr. Dara Childs

The present work investigates the phenomena of whip and whirl for a rigid rotor contacting at two bearing locations. The idea originated from an anemometer consisting of a rotor with an elastically supported stator undergoing the phenomena of dry friction whip and whirl at the two bushing contacts. To analyze the behavior, a mathematical model similar to the anemometer is developed and analyzed assuming two possible solutions, Mode1 (normal reaction forces in phase at two contacts) and Mode 2 (normal reaction forces out of phase at two contacts). Analytical solutions are only possible for the models with same RCl (Radius to Clearance ratio) at the two rub locations.

A simulation model is constructed using the Texas A&M University (TAMU) Turbomachinery Laboratory rotordynamics software suite XLTRC^2, comprised of Timoshenko beam finite elements to form multiple degrees of freedom rotor and stator models. The nonlinear connections at the rub surface are modeled using Hunt and Crossley’s contact model with coulomb friction. Dry friction simulations are performed for three separate models depending on the rotor’s mass disk location with respect to the contact locations. The three models used have (1) Disk at center location (2) Disk at ¾ location (3) Disk at overhang location.

The adequacy of the analytical solution is investigated using the above simulations. Also, cases are explored where the general assumed solution would not solve the mathematical model, e.g. different RCl ratios at the two contacts. Simulations are performed for increasing as well as decreasing running speeds.

There is partial agreement between simulation predictions and the analytical solutions for the cases with the mass center at centered and at ¾ location. First, whirl-to-whip transitions occur at near the combine rotor-stator bounce frequency for both disk at center and disk at ¾ location. The case with overhang mass disk predicts the two contacts to whip and at different frequencies simultaneously. Neither of the analytical solutions predicts a case where precession occurs at two different frequencies at the two contact points. Predictions for models with different RCl on the Backward Precessional (BP) graph *imitate* whirling. The BP graph predicts increasing BP frequency with increasing rotor speeds which is a characteristic of whirling, whereas investigation of individual contact velocities suggest that they are slipping at all conditions, one of them slipping more than the other netting a whirling like motion. For the overhang model with different RCl, apart from whipping at different frequency the two contacts also whirl at different frequencies corresponding to the RCl at the respective contacts.

Simulations for decreasing rotor speed predict jump down from whirl- to-whip different BP frequency as compared to the jump up from whip-to-whirl for the speed up

DEDICATION

Dedicated to my parents

ACKNOWLEDGEMENTS

I would like to express my sincere appreciation and gratitude to Dr. Dara Childs for his support and guidance. His exhaustive knowledge and insight in the field of rotordynamics has been a constant source of inspiration and has provided invaluable assistance during the course of research.

I am also greatly thankful to Dr. Palazzolo and Dr. Morgan for serving on my committee.

Thanks also go to my friends and colleagues and the department faculty and staff for making my time at Texas A&M University a great experience

Finally, thanks to my parents and my sister for their constant moral support.

NOMENCLATURE

Subscripts

s	Stator
r	Rotor
L	Left contact
R	Right contact
X	Along X in XZ plane
Y	Along Y in YZ plane

Symbols

$\boldsymbol{A}$	$\boldsymbol{Z_{sL}Z_{sR}} - (J_{s12}\Omega^2)^2$ as introduce in Eq.(20)	
a	Amplitude of rotor motion	[L]
c_{sL}, c_{rL}	Damping constants	[F t/L]
C_{rL},C_{rR}	Clearance at rub surface	[L]
D_w	$\boldsymbol{W_{11}W_{22}\text{-}W^2}$ as introduce in Eq.(27)	
$f_{rLX}, f_{rRX}, f_{rLY}\ f_{rRY}$	Reaction forces on the rotor at 2 contacts in the 2 planes	[F]
$f_L\ f_R$	Reaction forces in complex form	[F]
f_{fL}, f_{fR}	Friction force on rotor at two contacts	[F]
$K_{sL}, K_{rL},$	Stiffness constants	[F/L]
γ	Phase as introduced in Eq. 19	[-]
l_g	Position of rotor center of mass from origin illustrated in Figure 2(a) with respect to reference frame fixed to ground	[L]
l	Length of rotor between contact location	[L]
l_{sg}	Position of center of mass of stator with respect to origin illustrated in Figure 3(a) with respect to reference frame fixed to ground	[L]

l_s	Length of stator	[L]
m_s,m_r	Mass of stator/rotor	[M]
$N_{L,}$ N_R	Normal reaction on rotor at two contacts	[F]
ω	Rotor angular velocity	[1/t]
ω_{ns}	Stator natural frequency	[1/t]
ω_{nc}	Combined rotor stator natural frequency	[1/t]
Ω	Backward precessional velocity	[1/t]
r_{rLX} r_{rRX}, r_{rLY}, r_{rRY}	Rotor coordinates at the 2 contacts in the 2 planes	[L]
$\boldsymbol{r}_{rL}$ $\boldsymbol{r}_{rR}$	Rotor coordinates in complex form	[L]
r_{sLX} r_{sRX}, r_{sLY}, r_{sRY}	Stator coordinates at the 2 contacts in the 2 planes	[L]
$\boldsymbol{r}_{sR}$ $\boldsymbol{r}_{sR}$	Stator coordinates in complex form	[L]
$r_{Xc,}r_{Yc}$	Rotor coordinates of center of gravity	[L]
θ_{rY}, θ_{rX}	The rotor's inclination with respect to the horizontal and vertical axis	[-]

Abbreviations

BP	Backward precessional
RCl	Radius to clearance ratio

TABLE OF CONTENTS

Page

CHAPTER

LIST OF FIGURES

FIGURE Page

LIST OF TABLES

CHAPTER I

INTRODUCTION

Tighter Clearances have become inevitable due to the need for higher efficiency turbo machines, which can lead to rubbing between a rotor and a stator. Rubbing can lead to problems like wear of the surfaces in contact and vibrations in the machines. One of the more detrimental forms of vibration would arise when friction on the rotor from the stator cause the rotor to precess in a backward precessional motion. These can be very detrimental. Rosemblum [1] documents a case of dry-friction induced whirling motion that caused a catastrophic incident, which sheared a 600MW turbo generator at 16 places.

1.1 LITERATURE REVIEW

The first documented case of dry friction whip and whirl was by Newkirk [2] in 1926. He was studying rubbing interaction between a rotor and a stator when it started whirling in a direction opposite to the direction of shaft rotation. Following this occurrence Baker [3] and Den Hartog [4] in 1933 were able to derive the kinematic constraint which correlated the whirling frequency to the shaft speed.

Since then, attempts were made by different researchers to analytically explain the occurrence of backward precessing dry friction whip and whirl.

This thesis follows the style of ASME Journal of Vibration and Acoustics.

The most significant advancement to the dry friction whip and whirl model was made by Black [5,6] in 1967, 1968. Using a flexible rotor and an elastically supported stator, Black studied three types of rubbing interactions between the rotor and the stator.

(1) Synchronous rubbing with the rotor precessing at the running speed in the direction of the shaft rotation.

(2) Dry friction whirl in a direction opposite to the rotation of the shaft at a precession frequency based on the Radius-to-Clearance ratio (RCl) of the annulus between rotor and stator times the running speed.

(3) Dry friction whip in a direction opposite to the rotation of the shaft at a frequency approximately equal to the combined natural frequency of the rotor shaft system.

Black suggested that, if rotor and stator are forced to make contact by an external disturbance, dry friction will tend to induce rotor counter whirl. His model predicted counter whirl motion to be only possible between ranges of rotor/stator natural frequency and the next higher combined natural frequency. The U-shaped curves between friction angles and precession speed determined the feasibility of counter whirl. From these curves, he demonstrated that the shaft undergoes dry friction whirl and whip at comparatively low shaft speeds.

In 1990, Crandall [7] followed Black's lead to study the transition between dry fiction whirl and whip regimes. He used a simple Jeffcott rotor model. His findings for dry friction whip and whirl concurred with those of Black's. According to Crandall an external disturbance was required to initiate the dry friction whirl phenomena, and he determined the precession value of dry friction whip to be close to the critical speed of the combined rotor stator system.

The analytical solutions were tested out experimentally by researchers. The experiments by Lingener [8] and Choi [9], supported Black's predictions but test results from Bartha [10] and Yu et al. [11] seemed to contradict Black.

Lingener [8] used a flexible rotor with a mass that could be shifted and an elastically supported brass stator with adjustable stiffness for his test rig. He tested with different clearance values and variable stator stiffness on the shaft. He also tested for fixed stiffness and fixed clearance with the mass being attached to various locations. His results completely supported Black's model and Crandall's predictions as the whirling occurred at precession frequencies higher than the lowest natural frequency, of rotor and the upper limiting transition from whirl to whip being slightly lower than the lowest combined natural frequency. The only contradiction to Black's model was that Lingener could not traverse through any resonance of the joined system to reach a higher whirl regime predicted by Black.

Choi [9] carried out an experimental and numerical analysis for dry-friction whip and whirl. Unlike Lingener, Choi was able to traverse through the whip region, thus validating Black's prediction of possibility of returning to whirl after crossing a whip regime.

Bartha's [10] experimental results produced a lot of information on dry friction whip and whirl due to the test rig's capability to produce accurate excitation schemes using a high power active magnetic bearing. Bartha showed that the whirl solution is unstable at the transition to whip. In addition, Bartha cites a conflict between whirl ranges predicted using Black's dry-friction counter whirl model and those achieved experimentally.

Yu et al. [11] showed that an outside disturbance was not necessary to excite dry-friction whip. Instead, the occurrence was induced by synchronous response near a rotor critical speed. They stated that, once excited, whip can be sustained over a wide speed range until very slow speeds where slippage cannot be maintained. Also, they stated that their results contradicted Black's predictions.

In 2007, Childs and Bhattacharya [12] revisited Black's model to review his counter whirl approach in regard to result of Yu et al. and Bartha. The conclusions drawn from the results were:

1) Prediction of whip and whirl characteristics require an accurate rotor model. The number of rotor modes and location of contact points have a major influence over the accuracy.
2) Black's model had the sign term missing on the circumferential component of the reaction force. When included, the predictions from a nonlinear time transient model concurred with Bartha's/ Yu et al test results.
3) Predictions regarding multimode rotor-stator models caused formations of multiple U-shaped curves, thus showing several possible whirl regions. But in simulations only the first whirl range was produced.

Dyke [13] and Wilkes et al [14] designed and constructed a whip and whirl test rig that demonstrated and recorded accurately the nature of multi-mode dry-friction whip and whirl. The test-rig's drive system could deliver accurate acceleration and deceleration profiles while sustaining dry-friction instabilities. The test-rig design enabled testing of several rub surfaces to examine the effect of bearing material and clearance on dry-friction whip and whirl. Analysis of experimental data provided by the test rig revealed several interesting facets of dry-friction whip and whirl in a realistic machine. They found that the whip and whirl regions were not solely defined by rotor speed. The rotor speed was increased and decreased through regions characterized by whip, terminating with jumps to different whirl/whip frequencies. The whirl frequencies were in close proximity to the predicted whirl frequency which were roughly proportional to the RCl ratio at the contact locations. They found harmonic sidebands when analyzing the frequency spectrum. These harmonics became more prevalent in whip and sometimes led to excitation of higher whirl frequencies.

1.2 EVENTS LEADING TO 2- POINT CONTACT DRY FRICTION INVESTIGATION

In 2006, NRG systems [15] determined that some of their #40 anemometer sensors were exhibiting slowdown, a phenomena they termed dragging. In November 2007 customers requested them to conduct engineering evaluation on the faulty sensors. A large number of these sensors showed faulty post-calibration results.

A series of investigations were initiated to characterize the problem. Various tests to measure the characteristics of the affected sensors were done. The change in calibration values with time was seen to be quite prominent. Another test showed that the effected sensors exhibited a spirograph motion when observing the tip of the rotating anemometer head. The normal sensors did not exhibit these phenomena. With these observations in mind, NRG systems developed vibration monitoring equipment to test the faulty sensors. Tests showed that the faulty sensors did not follow the normal sensor vibration signature. They had a dominant vibration frequency separate from rotation speed. The spirograph motion was perceived as self excited vibratory phenomena. NRG systems then contacted Dr Dara Childs. He confirmed NRG's suspicion that the observed phenomenon was dry-friction whip.

NRG#40 has a rigid copper shaft with a mass disk at roughly its center. This rotor is supported on two Teflon bearing where rubbing occurs. The RCl was approximately 30 at the two contacts. This whole system is encased in an anemometer housing. To date, the analysis of dry friction whip and whirl is limited to single-point contact systems. NRG#40 is the first reported case of dry friction whip and whirl at two contact points. Such a case of rubbing at two contact locations has never been previously analyzed or modeled.

1.3 PREVIOUS WORK AND PROPOSED RESEARCH

Childs [16] subsequently developed a rotor-stator model with rubbing at two contact locations. The model consists of a rigid axisymmetric rotor and a rigid axisymmetric stator. The stator is supported to ground by elastic springs. The model's nominal axis of symmetry is the *Z* axis. Rubbing contact is possible across clearances at two axial locations. Two-dimensional motions are allowed in the *X* and *Y* directions for the rotor and the stator at both contact locations. The rotor has four degrees of freedom, namely displacements along the *X* and *Y* axes plus (small) rotations about these axes. The stator has only two displacement degrees of freedom (no pitch and yaw degrees of freedom). Gravity is neglected.

Assuming:(i) Contact always occurs at both locations, and (ii) The same clearance-to-radius ratio holds at both contact locations, he developed two separate solution modes. For Mode 1 solutions, motion at the two contact locations is in phase. For Mode 2 solutions, motion at the two contact locations is 180° out of phase. The solution approach basically follows Black [6]; producing the characteristic *U*-shaped curves for the level of Coulomb friction that is required to produce whirling contact (rolling without slipping).

Using Child's approach, a new model will be developed with four stator degrees of freedom, adding bounce and pitch rotations. Mode 1 and Mode 2 solutions will be developed for the model, continuing to use Child's assumptions that rubbing occurs at both locations, and the same RCl holds at both locations. The two mode have before been studied for retainer bearings by Kärkkäinen et al.[17] who investigated the effect of misalignment of these bearing causing a cylindrical (Mode1) or conical (Mode2) whirling motion of a rotor.

To investigate these predictions, the nonlinear model will be simulated using XLTRC2 software from the Turbomachinery Laboratory at Texas A&M University. The software numerically solves the model's equations of motion. Nonlinear interaction at the rub location will be modeled using a modified form of Hunt and Crossley's model [18].

The nonlinear model accounts for rotor and stator flexibility and can produce solutions for different clearance-to-radius ratios at the contact locations. The model will be used to investigate changes in parameters such as mass-center location, coefficient of friction, clearance-to-radius ratios, and contact stiffness. The three mass center locations to be considered are illustrated in figure 1.

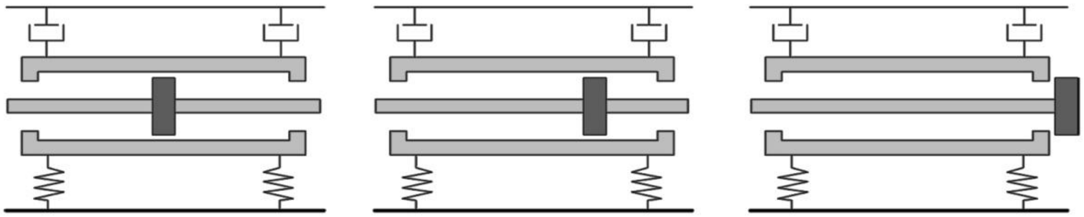

(A) *Mass in the center* (B) *Mass at 3/4th distance* (C) *Mass at overhang*

Figure 1 Model with Varied Rotor Disk Locations

CHAPTER II

MATHEMATICAL MODEL

2.1 TWO-POINT RUBBING CONTACT MODEL FOR A RIGID ROTOR SUPPORTED BY AN ELASTICALLY SUPPORTED RIGID STATOR

This analysis applies for rubbing contact between a rigid-body rotor and a four -degree–of-freedom stator that is supported by springs and dampers. Rubbing contact can occur between the rotor and stator at two different locations. Gravity is neglected.

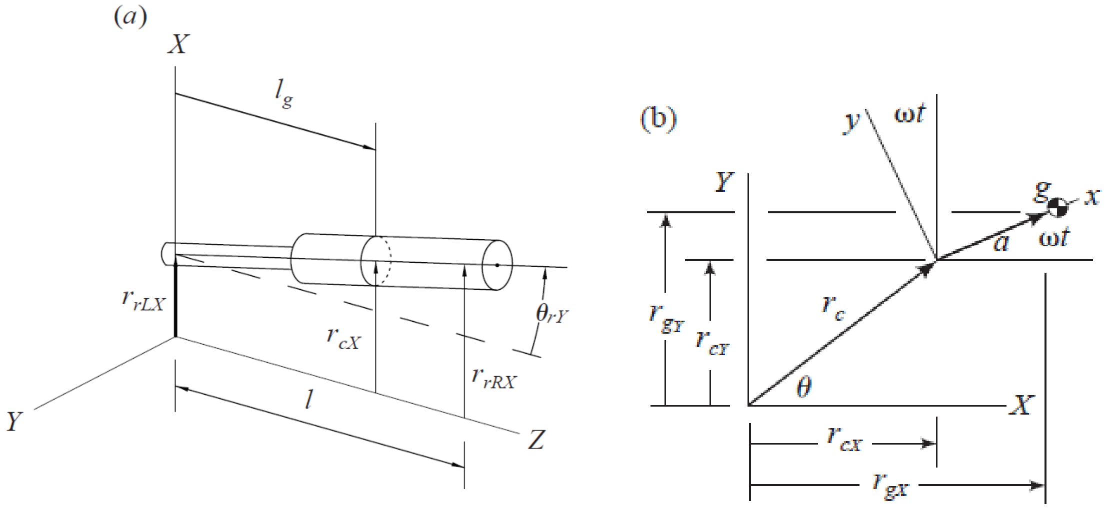

(a) Rotor Shaft

(b) Vector Representation of Rotor

Figure 2 Rotor Coordinates and Degree of Freedom

2.1.1 Rotor Equations of Motion

Child's[16] approach for finding the rotor stator equation for two contact points will now be reviewed.

Figure 2(a) illustrates a rotor temporarily located in the *X-Z* plane. It can contact at two locations with a point-mass stator (shown below). The left contact location will be identified with the subscript *L*, the right contact location with subscript *R*. The distance between contact locations is *l*. The vectors $\boldsymbol{r_{rL}}, \boldsymbol{r_{rR}}$ locate the rotor's axis at the left and right contact locations, respectively. The rotor's mass center lies in a plane perpendicular to the rotor's geometric axis that is displaced the axial distance l_g from the left contact location. Figure 1b shows the mass center position within a plane perpendicular to the Z axis located by $\boldsymbol{r_g} = \boldsymbol{I}r_{gX} + \boldsymbol{J}r_{gY}$ The rotor is rotating in the counter clockwise direction with angular velocity ω. The rotor's geometric center is located in this plane by $\boldsymbol{r_c} = \boldsymbol{I}r_{cX} + \boldsymbol{J}r_{cY}$. The rotor's mass center is displaced the distance '*a'* from its geometric axis. The vector's two components are related

$$r_{gX} = r_{cX} + a\cos\omega t \ , \ r_{gY} = r_{cY} + a\sin\omega t \tag{1}$$

The rotor's inclination with respect to the horizontal is defined by the (small) angle θ_{rY}. In the *X-Z* plane, the rotor's left and right positions at the contact with the stator are defined, respectively, by the displacement vectors $\boldsymbol{r_{rLX}}, \boldsymbol{r_{rRX}}$. They are related by:

$$\theta_{rY} = \frac{(r_{rRX} - r_{rLX})}{l}, \ r_{Xc} = r_{rLX} + \theta_{rY} l_g = r_{rLX} + \frac{l_g}{l}(r_{rRX} - r_{rLX}) = r_{rRX}\frac{l_g}{l} + r_{rLX}(1 - \frac{l_g}{l}) \tag{2}$$

In the *Y*-*Z* plane, the kinematic results is:

$$\theta_{rX} = \frac{(r_{rLY} - r_{rRY})}{l},\; r_{Yc} = r_{rLY} + \theta_{rX} l_g = r_{rLY} + \frac{l_g}{l}(r_{rRY} - r_{rLY}) = r_{rRY}\frac{l_g}{l} + r_{rLY}(1 - \frac{l_g}{l}) \tag{3}$$

The rotor’s kinetic energy is

$$\begin{aligned} T &= (\frac{m_r}{2}\dot{r}_{gX}^2 + \frac{I_{rg}}{2}\dot{\theta}_{rY}^2) + (\frac{m_r}{2}\dot{r}_{gY}^2 + \frac{I_{rg}}{2}\dot{\theta}_{rX}^2) \\ &= \frac{m_r}{2}[-a\omega \sin \omega t + \dot{r}_{rRX}\frac{l_g}{l} + \dot{r}_{rLX}(1 - \frac{l_g}{l})]^2 + \frac{I_{rg}}{2}[\frac{(\dot{r}_{rRX} - \dot{r}_{rLX})}{l}]^2 \\ &+ \frac{m_r}{2}[a\omega \cos \omega t + \dot{r}_{rRY}\frac{l_g}{l} + \dot{r}_{rLY}(1 - \frac{l_g}{l})]^2 + \frac{I_{rg}}{2}[\frac{(\dot{r}_{rLY} - \dot{r}_{rRY})}{l}]^2 \end{aligned}$$

Neglecting gravity, there is no potential energy, and Lagrange’s equations of motion nets

$$\begin{bmatrix} m_r(1 - \frac{l_g}{l})^2 + \frac{I_g}{l^2} & m_r\frac{l_g}{l}(1 - \frac{l_g}{l}) + \frac{I_g}{l^2} \\ m_r\frac{l_g}{l}(1 - \frac{l_g}{l}) + \frac{I_g}{l^2} & m_r(\frac{l_g}{l})^2 + \frac{I_g}{l^2} \end{bmatrix} \begin{Bmatrix} \ddot{r}_{rLX} \\ \ddot{r}_{rRX} \end{Bmatrix} = \begin{Bmatrix} f_{LX} + ma\omega^2 \cos \omega t(1 - \frac{l_g}{l}) \\ f_{RX} + ma\omega^2 \cos \omega t(\frac{l_g}{l}) \end{Bmatrix} \tag{4}$$

And

$$\begin{bmatrix} m_r(1 - \frac{l_g}{l})^2 + \frac{I_g}{l^2} & m_r\frac{l_g}{l}(1 - \frac{l_g}{l}) + \frac{I_g}{l^2} \\ m_r\frac{l_g}{l}(1 - \frac{l_g}{l}) + \frac{I_g}{l^2} & m_r(\frac{l_g}{l})^2 + \frac{I_g}{l^2} \end{bmatrix} \begin{Bmatrix} \ddot{r}_{rYL} \\ \ddot{r}_{rYR} \end{Bmatrix} = \begin{Bmatrix} f_{YL} + ma\omega^2 \cos \omega t(1 - \frac{l_g}{l}) \\ f_{YR} + ma\omega^2 \cos \omega t(\frac{l_g}{l}) \end{Bmatrix} \tag{5}$$

where f_{LX} , f_{LY} and f_{RX} , f_{RY} are the reaction-force components acting on the rotor at the left and right hand contact points, respectively. In condensed form, Eq. (4) and (5) can be combined as the single complex equation.

$$\begin{bmatrix} J_{r11} & J_r \\ J_r & J_{r22} \end{bmatrix} \begin{Bmatrix} \ddot{\boldsymbol{r}}_{\boldsymbol{rL}} \\ \ddot{\boldsymbol{r}}_{\boldsymbol{rR}} \end{Bmatrix} = \begin{Bmatrix} \boldsymbol{f_L} \\ \boldsymbol{f_R} \end{Bmatrix} + ma\omega^2 e^{\boldsymbol{j}\omega t} \begin{Bmatrix} (1-\frac{l_g}{l}) \\ (\frac{l_g}{l}) \end{Bmatrix} \tag{6}$$

Where

$$J_{r11} = [m_r(1-\frac{l_g}{l})^2 + \frac{I_{rg}}{l^2}] \text{ , } J_{r22} = [m_r(\frac{l_g}{l})^2 + \frac{I_{rg}}{l^2}] \text{ , } J_{\ r} = [m_r \frac{l_g}{l}(1-\frac{l_g}{l}) + \frac{I_{rg}}{l^2}]$$

$$\boldsymbol{r_{rL}} = r_{rXL} + \boldsymbol{j} r_{rYL}, \boldsymbol{r_{rR}} = r_{rXR} + \boldsymbol{j} r_{rYR}, \ \boldsymbol{f_L} = f_{XL} + \boldsymbol{j} r_{YL}, \ \boldsymbol{f_R} = f_{XR} + \boldsymbol{j} r_{YR} \tag{7}$$

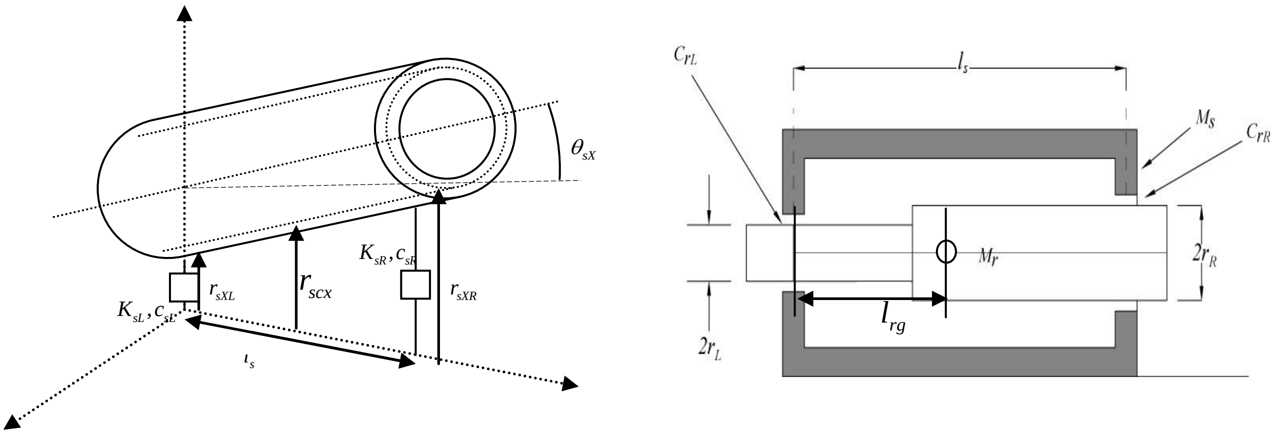

a) Stator

b) Section View Rotor and Stator Assembly

Figure 3 Stator Coordinates

2.1.2 Stator Equations of Motion

Using a similar approach, the stator equations of motion will be derived. Figure 3(b) illustrates the rotor and stator models, together but not contacting. The radial clearances at the left and right contact locations are C_{rR}, C_{rL} ; the corresponding rotor radii are r_{rR}, r_{rL}. The stator is allowed to pitch, yaw and bounce.

From Figure 3(a), θ_{sY} is defined in terms of r_{sLX}, r_{sRX} by

$$\theta_{sY} = \frac{(r_{sRX} - r_{sLX})}{l},\ r_{scX} = r_{sLX} + \theta_{sY} l_g = r_{sLX} + \frac{l_g}{l}(r_{sRX} - r_{sLX}) = r_{sRX}\frac{l_g}{l} + r_{sLX}(1 - \frac{l_g}{l}) \qquad (8)$$

In the *Y-Z* plane, the kinematic result is:

$$\theta_{sX} = \frac{(r_{sYL} - r_{sYR})}{l},\ r_{scY} = r_{sYL} + \theta_{sX} l_g = r_{sYL} + \frac{l_g}{l}(r_{sYR} - r_{sYL}) = r_{sYR}\frac{l_g}{l} + r_{sYL}(1 - \frac{l_g}{l}) \qquad (9)$$

The stator's kinetic energy is

$$\begin{aligned} T &= (\frac{m_s}{2}\dot{r}_{sXc}^2 + \frac{I_{sg}}{2}\dot{\theta}_{sY}^2) + (\frac{m_s}{2}\dot{r}_{sYc}^2 + \frac{I_{sg}}{2}\dot{\theta}_{sX}^2) \\ &= \frac{m_s}{2}[-a\omega\sin\omega t + \dot{r}_{sRX}\frac{l_{sg}}{l_s} + \dot{r}_{sLX}(1 - \frac{l_{sg}}{l_s})]^2 + \frac{I_{sg}}{2}[\frac{(\dot{r}_{sRX} - \dot{r}_{sLX})}{l_s}]^2 \\ &+ \frac{m_s}{2}[a\omega\cos\omega t + \dot{r}_{sRY}\frac{l_{sg}}{l_s} + \dot{r}_{sLY}(1 - \frac{l_{sg}}{l_s})]^2 + \frac{I_{sg}}{2}[\frac{(\dot{r}_{sLY} - \dot{r}_{sRY})}{l_s}]^2 \end{aligned}$$

The stator's Potential energy is

$$U = \left(\frac{K_{sL}}{2}r_{sLX}^2 + \frac{K_{sR}}{2}r_{sRX}^2\right) + \left(\frac{K_{sL}}{2}r_{sLY}^2 + \frac{K_{sR}}{2}r_{sRY}^2\right)$$

The stator’s Rayleigh dissipation function is

$$\Im = \left(\frac{c_{sL}}{2} \dot{r}_{sLX}^2 + \frac{c_{sR}}{2} \dot{r}_{sRX}^2 \right) + \left(\frac{c_{sL}}{2} \dot{r}_{sLY}^2 + \frac{c_{sR}}{2} \dot{r}_{sRY}^2 \right)$$

For the stator Lagrange’s equations of motion nets

$$\begin{bmatrix} m_s (1-\frac{l_g}{l})^2 + \frac{I_{sg}}{l^2} & m_s \frac{l_{sg}}{l}(1-\frac{l_g}{l}) + \frac{I_{sg}}{l^2} \\ m_s \frac{l_g}{l}(1-\frac{l_g}{l}) + \frac{I_{sg}}{l^2} & m_s (\frac{l_{sg}}{l})^2 + \frac{I_{sg}}{l^2} \end{bmatrix} \begin{Bmatrix} \ddot{r}_{rLX} \\ \ddot{r}_{rRX} \end{Bmatrix} + \begin{bmatrix} c_{sL} & 0 \\ 0 & c_{sR} \end{bmatrix} \begin{Bmatrix} \dot{r}_{rLX} \\ \dot{r}_{rRX} \end{Bmatrix} + \begin{bmatrix} K_{sL} & 0 \\ 0 & K_{sR} \end{bmatrix} \begin{Bmatrix} r_{rLX} \\ r_{rRX} \end{Bmatrix}$$

$$= -\begin{Bmatrix} f_{LX} \\ f_{RX} \end{Bmatrix} \tag{10}$$

and

$$\begin{bmatrix} m_s (1-\frac{l_g}{l})^2 + \frac{I_{sg}}{l^2} & m_s \frac{l_{sg}}{l}(1-\frac{l_g}{l}) + \frac{I_{sg}}{l^2} \\ m_s \frac{l_g}{l}(1-\frac{l_g}{l}) + \frac{I_{sg}}{l^2} & m_s (\frac{l_{sg}}{l})^2 + \frac{I_{sg}}{l^2} \end{bmatrix} \begin{Bmatrix} \ddot{r}_{rLY} \\ \ddot{r}_{rRY} \end{Bmatrix} + \begin{bmatrix} c_{sL} & 0 \\ 0 & c_{sR} \end{bmatrix} \begin{Bmatrix} \dot{r}_{rLY} \\ \dot{r}_{rRY} \end{Bmatrix} + \begin{bmatrix} K_{sL} & 0 \\ 0 & K_{sR} \end{bmatrix} \begin{Bmatrix} r_{rLY} \\ r_{rRY} \end{Bmatrix}$$

$$= -\begin{Bmatrix} f_{LY} \\ f_{RY} \end{Bmatrix} \tag{11}$$

In complex format, they become

$$\begin{bmatrix} J_{s11} & J_s \\ J_s & J_{s22} \end{bmatrix} \begin{Bmatrix} \ddot{\boldsymbol{r}}_{\boldsymbol{rL}} \\ \ddot{\boldsymbol{r}}_{\boldsymbol{rR}} \end{Bmatrix} + \begin{bmatrix} c_{sL} & 0 \\ 0 & c_{sR} \end{bmatrix} \begin{Bmatrix} \dot{\boldsymbol{r}}_{\boldsymbol{rL}} \\ \dot{\boldsymbol{r}}_{\boldsymbol{rR}} \end{Bmatrix} + \begin{bmatrix} K_{sL} & 0 \\ 0 & K_{sR} \end{bmatrix} \begin{Bmatrix} \boldsymbol{r}_{\boldsymbol{rL}} \\ \boldsymbol{r}_{\boldsymbol{rR}} \end{Bmatrix} = -\begin{Bmatrix} \boldsymbol{f}_{\boldsymbol{L}} \\ \boldsymbol{f}_{\boldsymbol{R}} \end{Bmatrix} \tag{12}$$

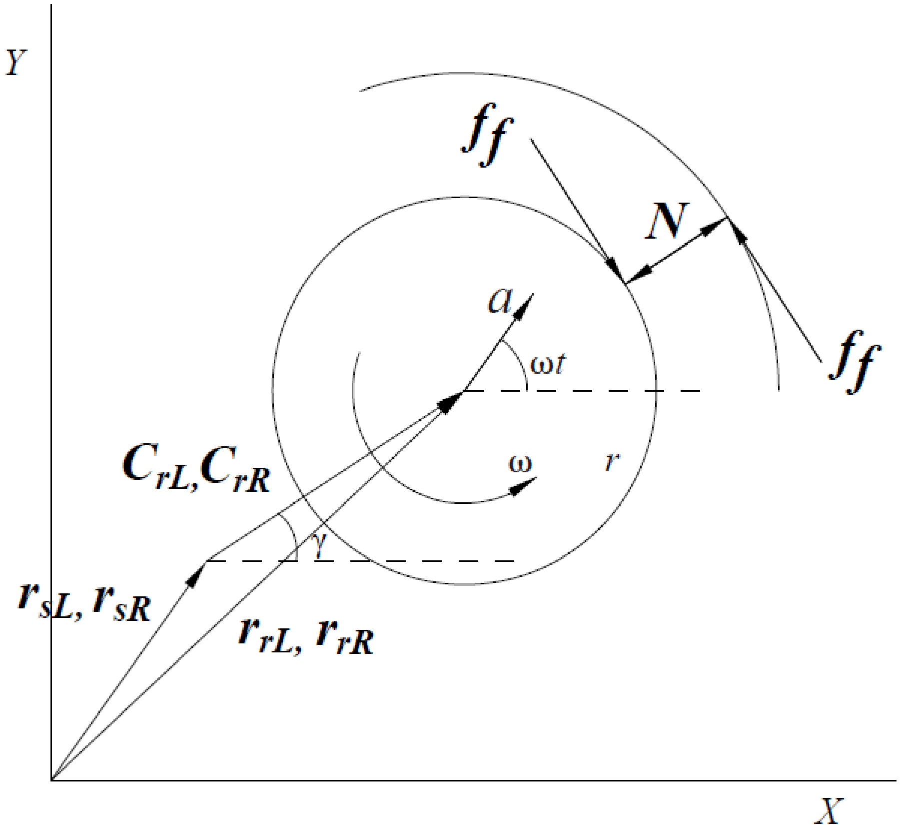

Figure 4 Clearance Diagram (Constraints)

2.1.3 Constraint Equations

Figure 4 illustrates the contact reaction forces and geometry relations between the rotor and stator displacement vectors at either contact location. From this figure, the constraint equations at the left and right contact points are

$$C_{rR}e^{j\gamma_r} = \boldsymbol{r_{rR}} - \boldsymbol{r_{sR}} \ , \ C_{rL}e^{j\gamma_l} = \boldsymbol{r_{rL}} - \boldsymbol{r_{sL}} \tag{13}$$

2.2 CONTACT FORCES -MODE 1

For this mode, we assume a planar precessing mode with the normal reaction contact forces $\boldsymbol{N_L}, \boldsymbol{N_R}$ in phase at the two contact points; hence, $\gamma_l = \gamma_R = \gamma$. Note: This equation does not require that the *motion* be in phase at the contact points; i.e., $\boldsymbol{r_{rL}}$ and $\boldsymbol{r_{rR}}$ are not necessarily in phase. The contact force components at the contact points are

$$\begin{aligned} f_{rLX} &= -N_L \cos\gamma + f_{fL} \sin\gamma \ , \ f_{rLY} = -N_L \sin\gamma - f_{fL} \cos\gamma \\ f_{rRX} &= -N_R \cos\gamma + f_{fR} \sin\gamma \ , \ f_{rRY} = -N_R \sin\gamma - f_{fR} \cos\gamma \end{aligned} \tag{14}$$

For this result,

$$\begin{aligned} \boldsymbol{f_L} &= -N_L(\cos\gamma + \boldsymbol{j}\sin\gamma) + f_{fL}(\cos\gamma - \boldsymbol{j}\sin\gamma) = -(N_L + \boldsymbol{j}f_{fL})e^{\boldsymbol{j}\gamma} \\ \boldsymbol{f_R} &= -(N_R + \boldsymbol{j}f_{fR})e^{\boldsymbol{j}\gamma} \end{aligned} \tag{15}$$

Neglecting the influence of imbalance, the rotor equations of motion become

$$\begin{bmatrix} J_{r11} & J_r \\ J_r & J_{r22} \end{bmatrix} \begin{Bmatrix} \ddot{\boldsymbol{r}}_{\boldsymbol{rL}} \\ \ddot{\boldsymbol{r}}_{\boldsymbol{rR}} \end{Bmatrix} = -\begin{Bmatrix} (N_L + \boldsymbol{j}f_{fL}) \\ (N_R + \boldsymbol{j}f_{fR}) \end{Bmatrix} e^{\boldsymbol{j}\omega t} \tag{16}$$

Solving Eq (16) for the accelerations nets

$$\begin{aligned} \ddot{\boldsymbol{r}}_{\boldsymbol{rL}} &= -\frac{l^2}{I_{rg}m_r}[J_{r22}(N_L + \boldsymbol{j}f_{fL}) - J_r(N_R + \boldsymbol{j}f_{fR})]e^{\boldsymbol{j}\gamma} \\ \ddot{\boldsymbol{r}}_{\boldsymbol{rR}} &= -\frac{l^2}{I_{rg}m_r}[J_{r11}(N_R + \boldsymbol{j}f_{fR}) - J_r(N_L + \boldsymbol{j}f_{fL})]e^{\boldsymbol{j}\gamma} \end{aligned} \tag{17}$$

Eq. (12), (16) the stator equations of motion in complex form, become:

$$\begin{bmatrix} J_{s11} & J_s \\ J_s & J_{s22} \end{bmatrix} \begin{Bmatrix} \ddot{\boldsymbol{r}}_{\boldsymbol{rL}} \\ \ddot{\boldsymbol{r}}_{\boldsymbol{rR}} \end{Bmatrix} + \begin{bmatrix} c_{sL} & 0 \\ 0 & c_{sR} \end{bmatrix} \begin{Bmatrix} \dot{\boldsymbol{r}}_{\boldsymbol{rL}} \\ \dot{\boldsymbol{r}}_{\boldsymbol{rR}} \end{Bmatrix} + \begin{bmatrix} K_{sL} & 0 \\ 0 & K_{sR} \end{bmatrix} \begin{Bmatrix} \boldsymbol{r}_{\boldsymbol{rL}} \\ \boldsymbol{r}_{\boldsymbol{rR}} \end{Bmatrix} = \begin{Bmatrix} (N_L + \boldsymbol{j} f_{fL}) \\ (N_R + \boldsymbol{j} f_{fR}) \end{Bmatrix} \tag{18}$$

$$J_{s11} = [m_s (1 - \frac{l_{sg}}{l_s})^2 + \frac{I_{sg}}{l_s^2}]\ ,\ J_{s22} = [m_s (\frac{l_{sg}}{l_s})^2 + \frac{I_{sg}}{l_s^2}]\ ,\ J_s = [m_s \frac{l_g}{l_s} (1 - \frac{l_g}{l_s}) + \frac{I_{sg}}{l_s^2}]$$

.

We assume a whirling precession solution of the form:

$$\begin{aligned} \boldsymbol{r}_{\boldsymbol{sL}} &= \boldsymbol{r}_{\boldsymbol{sL0}} e^{\boldsymbol{j}(\gamma_0 - \Omega t)} \qquad & \boldsymbol{r}_{\boldsymbol{rL}} &= \boldsymbol{r}_{\boldsymbol{rL0}} e^{\boldsymbol{j}(\gamma_0 - \Omega t)} \\ \boldsymbol{r}_{\boldsymbol{sR}} &= \boldsymbol{r}_{\boldsymbol{sR0}} e^{\boldsymbol{j}(\gamma_0 - \Omega t)} \qquad & \boldsymbol{r}_{\boldsymbol{rR}} &= \boldsymbol{r}_{\boldsymbol{rR0}} e^{\boldsymbol{j}(\gamma_0 - \Omega t)} \end{aligned} \tag{19}$$

With precession in the clockwise direction at the rate Ω (opposite to the shaft rotation direction ω). Substituting from Eq. (19) into Eq. (18) produces:

$$\begin{aligned} \boldsymbol{r}_{\boldsymbol{rR0}} &= \frac{l^2}{I_{rg} m_r \Omega^2} [J_{r11} (N_R + \boldsymbol{j} f_{fR}) - J_r (N_L + \boldsymbol{j} f_{fL})] \\ \boldsymbol{r}_{\boldsymbol{rL0}} &= \frac{l^2}{I_{rg} m_r \Omega^2} [J_{r22} (N_L + \boldsymbol{j} f_{fL}) - J_r (N_R + \boldsymbol{j} f_{fR})] \\ \boldsymbol{r}_{\boldsymbol{sL0}} &= \frac{(N_L + \boldsymbol{j} f_{fL}) Z_{sR} + J_s \Omega^2 (N_R + \boldsymbol{j} f_{fR})}{\boldsymbol{A}} \\ \boldsymbol{r}_{\boldsymbol{sR0}} &= \frac{(N_R + \boldsymbol{j} f_{fR}) Z_{sL} + J_s \Omega^2 (N_L + \boldsymbol{j} f_{fL})}{\boldsymbol{A}} \end{aligned} \tag{20}$$

where

$$\begin{aligned}&\boldsymbol{A} = \boldsymbol{Z_{sL}}\boldsymbol{Z_{sR}} - (J_{s12}\Omega^2)^2\\ &\boldsymbol{Z_{sL}} = (k_{sL} - J_{s11}\Omega^2) - \boldsymbol{j}\Omega c_{sL}\ ,\ \boldsymbol{Z_{sR}} = (k_{sR} - J_{s22}\Omega^2) - \boldsymbol{j}\Omega c_{sR}\end{aligned} \tag{21}$$

Similarly, the constraint Eq. (13) becomes

$$\begin{aligned}\boldsymbol{C_{rR}} &= \boldsymbol{r_{rR0}} - \boldsymbol{r_{sR0}}\\ \boldsymbol{C_{rL}} &= \boldsymbol{r_{rL0}} - \boldsymbol{r_{sL0}}\end{aligned} \tag{22}$$

Substituting for $\boldsymbol{r_{rL0}}, \boldsymbol{r_{rR0}}, \boldsymbol{r_{sL0}}, \boldsymbol{r_{sR0}}$ into Eq. (22) gives

$$\begin{aligned}C_{rL} &= (N_L + \boldsymbol{j}f_{fL})[\frac{J_{r22}l^2}{I_g m_r\Omega^2} - \frac{\boldsymbol{Z_{sR}}}{\boldsymbol{A}}] - (N_R + \boldsymbol{j}f_{fR})[\frac{J_r l^2}{I_g m_r\Omega^2} + \frac{J_s\Omega^2}{\boldsymbol{A}}]\\ C_{rR} &= -(N_L + \boldsymbol{j}f_{fL})[\frac{J_r l^2}{I_g m_r\Omega^2} + \frac{J_s\Omega^2}{\boldsymbol{A}}] + (N_R + \boldsymbol{j}f_{fR})[\frac{J_{r11}l^2}{I_g m_r\Omega^2} - \frac{\boldsymbol{Z_{sL}}}{\boldsymbol{A}}]\end{aligned} \tag{23}$$

The reaction forces $N_L + \boldsymbol{j}f_{fL}$, $N_R + \boldsymbol{j}f_{fR}$ are a function of the precession frequency Ω and are defined by

$$\begin{bmatrix}\boldsymbol{W_{11}} & \boldsymbol{-W}\\ \boldsymbol{-W} & \boldsymbol{W_{22}}\end{bmatrix}\begin{bmatrix}N_L + \boldsymbol{j}f_{fL}\\ N_R + \boldsymbol{j}f_{fR}\end{bmatrix} = \begin{bmatrix}C_{rL}\\ C_{rR}\end{bmatrix} \tag{24}$$

where

$$\boldsymbol{W_{11}} = [\frac{J_{r22}l^2}{I_g m_r\Omega^2} - \frac{\boldsymbol{Z_{sR}}}{\boldsymbol{A}}]\ ,\ \boldsymbol{W} = [\frac{J_r l^2}{I_g m_r\Omega^2} + \frac{J_s\Omega^2}{\boldsymbol{A}}]\ ,\ \boldsymbol{W_{22}} = [\frac{J_{r11}l^2}{I_g m_r\Omega^2} - \frac{\boldsymbol{Z_{sL}}}{\boldsymbol{A}}] \tag{25}$$

The solution to Eq. (24) is

$$\begin{aligned}(N_L + \boldsymbol{j}f_{fL}) &= \frac{C_{rL}\boldsymbol{W_{22}} + C_{rR}\boldsymbol{W}}{\boldsymbol{D_W}} \\ (N_R + \boldsymbol{j}f_{fR}) &= \frac{C_{rR}\boldsymbol{W_{11}} + C_{rL}\boldsymbol{W}}{\boldsymbol{D_W}}\end{aligned} \tag{26}$$

where

$$\boldsymbol{D_W} = \boldsymbol{W_{11}W_{22}} - \boldsymbol{W}^{\boldsymbol{2}} \tag{27}$$

Note that ω_{nc} is the undamped natural frequency for the rotor and stator pinned together. The natural frequency of the unsupported rotor is $\omega_{nr} = 0$, either from the displacement root associated with $m_r\Omega^2$ or the pitch/yaw motion associated with $I_g\Omega^2$. The stator's undamped natural frequency is $\omega_{ns} > \omega_{nc}$

Evaluating the reaction forces in Eq.(26) will produce the normal reaction magnitudes N_L, N_R and friction restraint force magnitudes f_{fL}, f_{fR}, netting the required Coulomb-friction factors;

$$\mu_{Lrequired}(\Omega) = \frac{f_{fL}}{N_L}\ ,\ \mu_{Rrequired}(\Omega) = \frac{f_{fR}}{N_R} \tag{28}$$

Contact between the rotor and stator at the left and right locations requires

$$N_L(\Omega) > 0\ ,\ N_R(\Omega) > 0 \tag{29}$$

Note that contact is possible at one location while absent at the other, for example $N_L > 0, N_R = 0$. Rolling without slipping requires

$$0 \le \mu_{Lrequired} \le \mu_L \ , \ 0 \le \mu_{Rrequired} \le \mu_R \tag{30}$$

Where μ_L, μ_R are the available static Coulomb damping coefficients at the left and right contact locations. Again, with contact at both locations, slipping can occur at one of the two contact surfaces with rolling-without slipping at the other.

For the single-contact models of Black and Crandall, contact was not possible $(N \le 0)$ for $0 < \Omega < \omega_{nr}$, becoming possible for $\omega_{nr} < \Omega < \omega_{nc}$.Within this precession-frequency band, rolling without slipping was predicted for $0 \le \mu_{required} \le \mu$, yielding Black's 'U-shaped', $\mu_{required}$ versus Ω curves. For rolling without slipping, the running speed ω and precessional frequency Ω are related by $\Omega = (r / C_r)\omega$ producing a 'tracking' super synchronous response. Whipping initiated for $\Omega = \omega_{nc}$ with a super synchronous response fixed at ω_{nc} for increasing speed ω. For $\Omega > \omega_{ns}$, whirling motion was again possible.

For $c = 0$ (damping=0) and $\Omega = \omega_{nc}$, contact and slipping (whip) will occur at both contact locations. Whip is predicted whether $r_L / C_{rL} = r_R / C_{rR}$ or $r_L / C_{rL} \ne r_R / C_{rR}$. If $r_L / C_{rL} = r_R / C_{rR}$, then the corresponding running speed during whirl is

$\omega = r_L\Omega / C_{rL} = r_R\Omega / C_{rR}$. However, if $r_L / C_{rL} \neq r_R / C_{rR}$ and whirling is occurring at one location, then slipping will be required at the other location.

2.3 ANALYTICAL PREDICTIONS FOR MODE 1

The following numerical values were used for prediction of backward precessional whip and whirl characteristics for the two point contact model.

$$l = .29\ m\ ;\ l_s = .27\ m$$

$$K_{sL} = K_{sR} = 4.70\text{E+06}\,\text{N/m}$$

$$c_{sL} = c_{sR} = 324.9\,\text{N-s/m}$$

$$C_{rR} = C_{rL} = 3.81E - 04\ \text{m} \tag{31}$$

$$r_{rL} = r_{rR} = 3.81\text{E} - 02\,\text{m}$$

$$I_g = .029\ kgm^2\ \ ,\ I_{sg} = .206\ kgm^2$$

$$m_s = 21.44\ kg\ \ ,\ m_r = 9.99\ kg$$

$$\mu = .5$$

2.3.1 Disk at Center- Mode 1

Using the equations of motion, the undamped stator and rotor-stator pinned natural frequencies were calculated as follows.

$$\omega_{ns}(bounce) = 105.3\text{Hz},\ \omega_{ns}(pitch) = 144.9\text{Hz}$$

$$\omega_{nc}(bounce) = 87.03\text{Hz},\ \omega_{nc}(pitch) = 135.5\text{Hz}$$

Equation (26) can be used to define a relation for the friction coefficient. Plotting the coefficient of friction as a function of the whirl frequencies, thereby establishing frequency ranges with enough friction co-efficient to sustain dry friction whirl. Black in his study of single point contact interaction concluded that whirling occurred between individual (rotor/stator) frequencies and the next combined natural frequencies. A similar result is seen in the Figure (5). The whirling range starts from zero because the rotor has a zero natural frequency due to lack of elastic support.

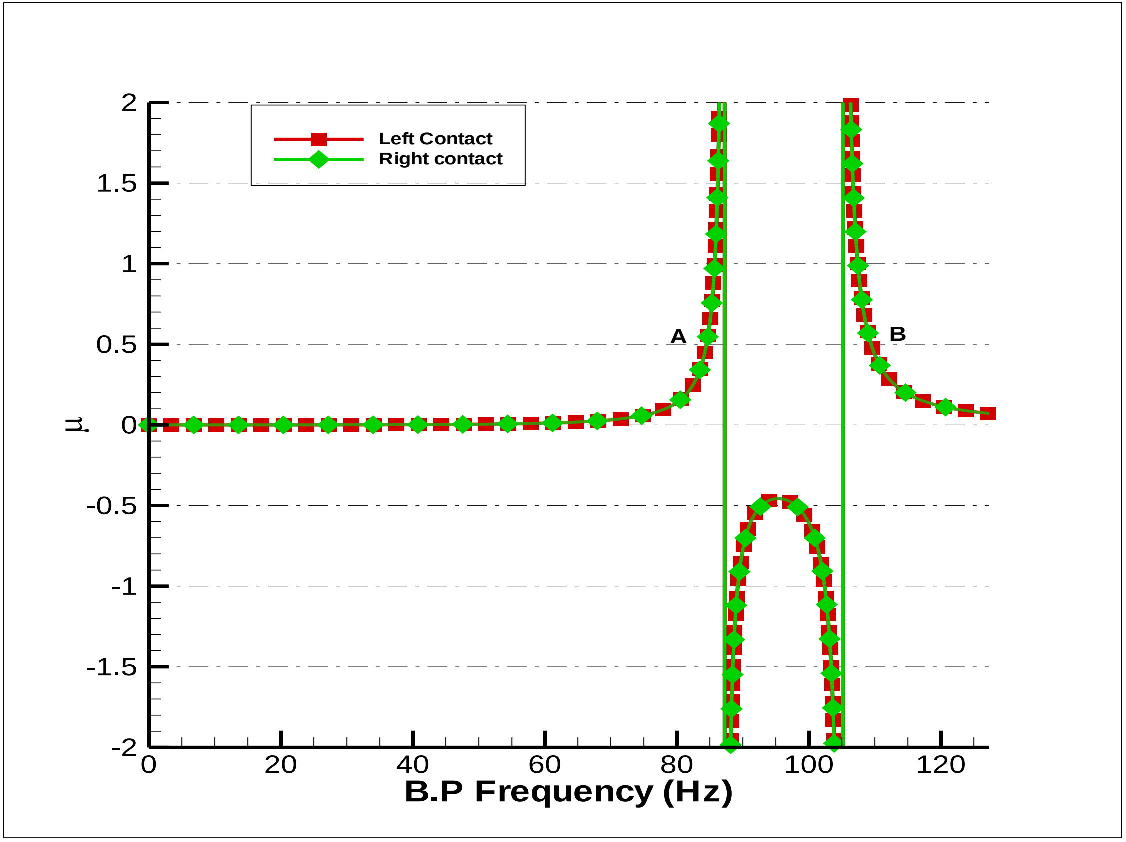

Figure 5 Disk at Center $RCl_L = RCl_R = 100$-Mode 1

As seen in Figure 5, the two limiting whirl frequencies of 87.3Hz and 105 Hz are the combined rotor stator natural frequencies and stator natural frequency respectively. But in reality whirl will be expected only till 84.5 and then beyond109.4 because beyond those values $\mu_{req>}\mu=0.5$

Position A separates a whirl solution on the left from an unattainable solution on the right. A reduction of speed reduces the coefficient of friction thus decreasing the whirl frequency. However an increase in speed leads to loss in traction yielding a slip or a whip condition. The range between the combined and stator natural frequencies has a negative friction coefficient. For this range, the solution cannot be predicted. A whip or loose contact is expected.

From the point of reentry denoted by point B increasing shaft speed reduces the required friction coefficient; decreasing shaft speed however increases the required friction coefficient subsequently decreasing whirl frequency, hence Point B is an unstable solution.

The solution is thus supposed to whirl up to point A, whip between points A and B and whirl again above Point B, since $\mu_{req=}\mu$

2.3.2 Disk at ¾ Location- Mode 1

Using the equations of motion, and the data of E.g. (31, the stator and rotor-stator combined natural frequencies for a disk at ¾ location were calculated as follows.

$$\omega_{ns}(bounce)=105.3\text{Hz},\ \omega_{ns}(pitch)=144.9\text{Hz}$$
$$\omega_{nc}(bounce)=87.03\text{Hz},\ \omega_{nc}(pitch)=132.6\text{Hz}$$

Eq. (26) holds true for the disk at ¾ location, since moving the disk only changes the rotor configurations by changing its center of gravity, thus changing the value of l_g (rotor center of gravity location) from .145m to .22m and value of I_g (moment of inertia) to .04kgm^2 from .02 kgm^2.

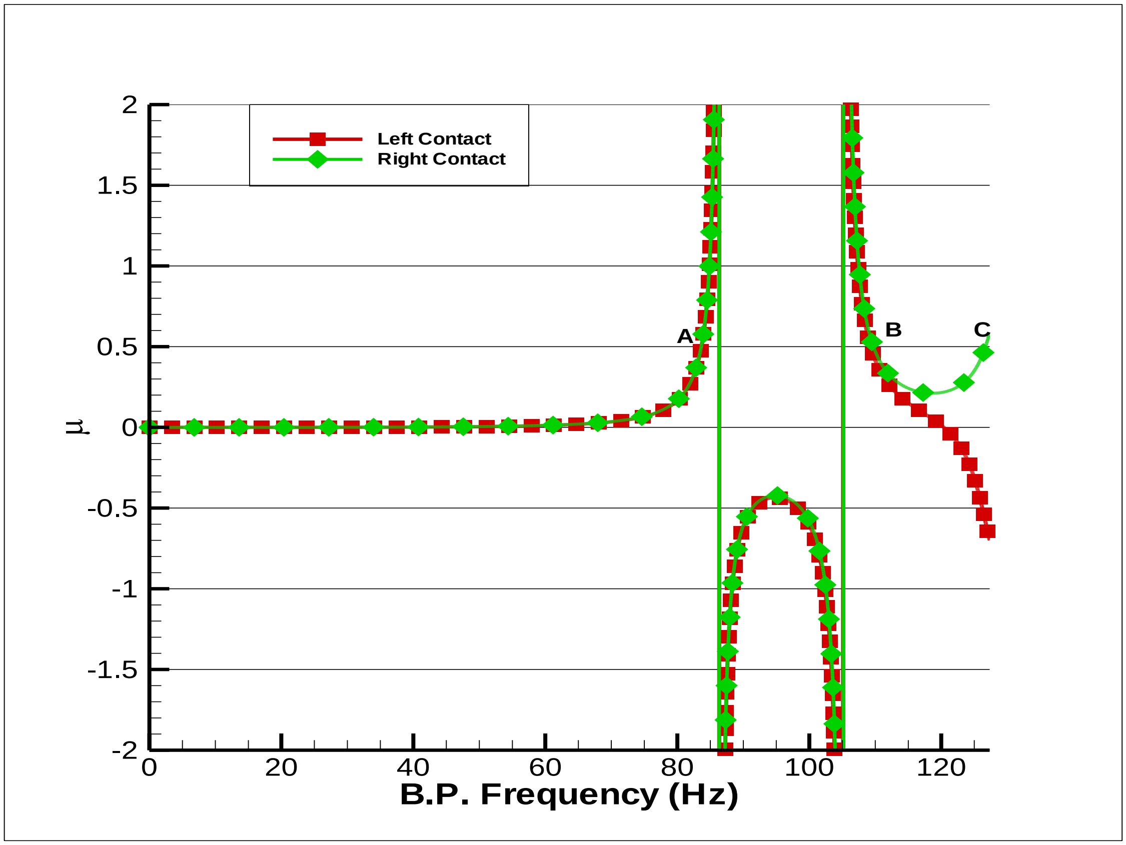

Figure 6 Disk at ¾ Location RCl$_L$= RCl$_R$=100. Mode 1

Figure 6 shows a very similar plot as for the centered mass disk. The whirl region extends from zero to the combined natural frequency corresponding to the present configurations of 87Hz. The slight difference from the calculated natural frequency could be arising due to presence of damping, which seems to be affecting non symmetric (disk at position other than center) cases. Again, whirling would be expected till point A, 83.66 Hz because beyond this μ_{req} exceeds μ It then transitions to whip. The next region (between B and C) the right contact undergoes a whirling solution but the left contact whirls for the first half and whips for the second half of this region.

2.3.3 Disk at Overhang Location- Mode 1

Using the data in e.g. (31), the calculated values of undamped natural frequencies using are:

$$\omega_{ns}(bounce) = 105.3\text{Hz},\ \omega_{ns}(pitch) = 144.9\text{Hz}$$
$$\omega_{nc}(bounce) = 87.03\text{Hz},\ \omega_{nc}(pitch) = 123\text{Hz}$$

For the overhang model the disk is shifted to a point beyond the right contact . The center of gravity hence shifts to a position .26m from .145m. Using the I_g =.07 we can make predictions for disk at overhang position.

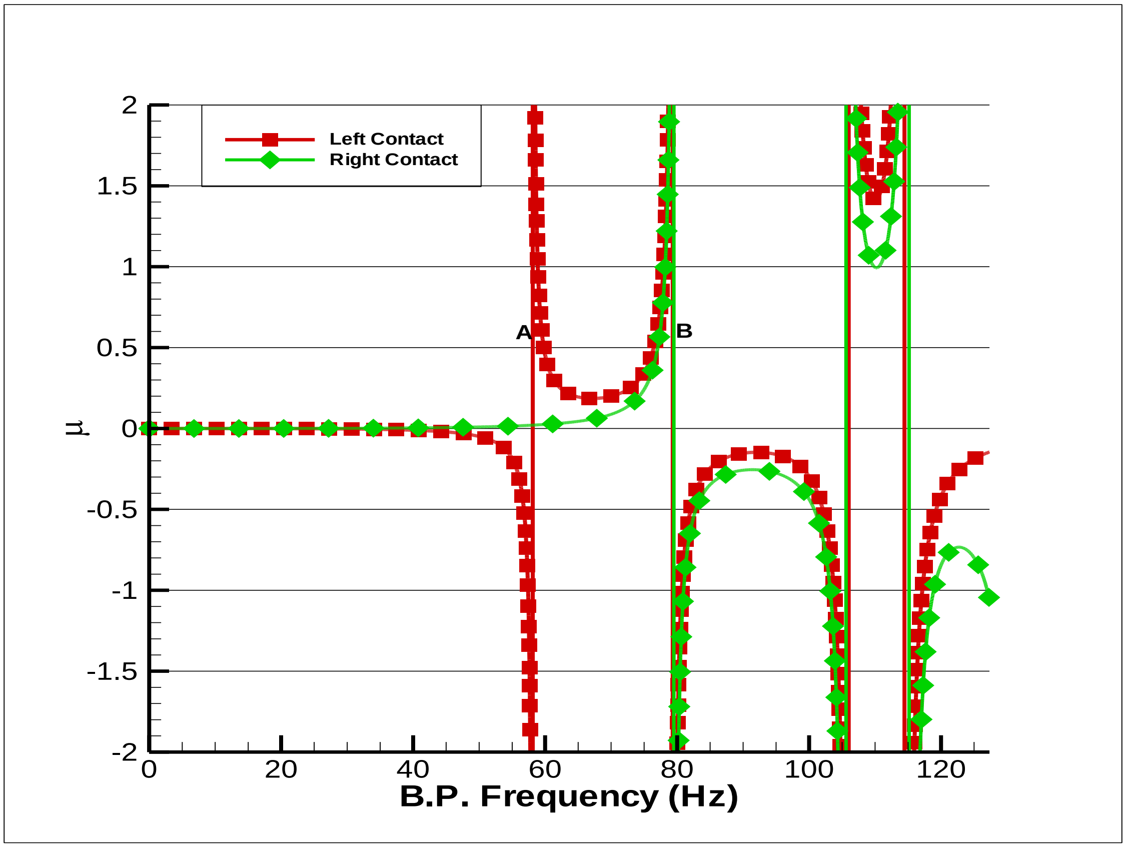

Figure 7 Disk at Overhang Location RCl$_L$= RCl$_R$=100. Mode 1

Figure7 predicts that the left contact will whirl between A and B, whereas the right contact whirls from 0 to B. No other whirling range is seen in this model. A small positive region of positive μ is seen between 105 and 117 Hz, but it never reaches the required μ of .5; hence, no whirling is expected

2.4 CONTACT FORCES — MODE 2

For this mode, we assume a planar precessing mode with *normal contact forces* 180° out of phase; hence $\gamma_L = \gamma, \gamma_R = \gamma + \pi$. This stipulation does not produce *motion* that is out of phase at the two contact locations; i.e. $\boldsymbol{r}_{\boldsymbol{rL}}$ and $\boldsymbol{r}_{\boldsymbol{rR}}$ are not necessarily 180° out of phase. The contact force components at the left and right contact locations are

$$\begin{aligned} f_{rXL} &= -N_L \cos\gamma + f_{fL}\sin\gamma \ , \ f_{rYL} = -N_L \sin\gamma - f_{fL}\cos\gamma \\ f_{rXR} &= N_R \cos\gamma - f_{fR}\sin\gamma \ , \ f_{rYR} = N_R \sin\gamma + f_{fR}\cos\gamma \end{aligned} \tag{32}$$

In complex form, they become

$$\begin{aligned} \boldsymbol{f}_L &= -(N_L + \boldsymbol{j} f_{fL})e^{\boldsymbol{j}\gamma} \\ \boldsymbol{f}_{\boldsymbol{R}} &= (N_R + \boldsymbol{j} f_{fR})e^{\boldsymbol{j}\gamma} \end{aligned} \tag{33}$$

Eq. (6) for the rotor becomes

$$\begin{bmatrix} J_{r11} & J_r \\ J_r & J_{r22} \end{bmatrix} \begin{Bmatrix} \ddot{\boldsymbol{r}}_{\boldsymbol{rL}} \\ \ddot{\boldsymbol{r}}_{\boldsymbol{rR}} \end{Bmatrix} = \begin{Bmatrix} -(N_L + \boldsymbol{j} f_{fL}) \\ (N_R + \boldsymbol{j} f_{fR}) \end{Bmatrix} e^{\boldsymbol{j}\gamma} + ma\omega^2 e^{\boldsymbol{j}\omega t} \begin{Bmatrix} (1 - \dfrac{\lg}{l}) \\ (\dfrac{\lg}{l}) \end{Bmatrix} \tag{34}$$

Neglecting imbalance, the acceleration impacts are:

$$\begin{aligned} \ddot{\boldsymbol{r}}_{\boldsymbol{rL}} &= -\frac{l^2}{I_g m_r}[J_{r22}(N_L + \boldsymbol{j} f_{fL}) + J_r(N_R + \boldsymbol{j} f_{fR})]e^{\boldsymbol{j}\gamma} \\ \ddot{\boldsymbol{r}}_{\boldsymbol{rR}} &= \frac{l^2}{I_g m_r}[J_{r11}(N_R + \boldsymbol{j} f_{fR}) + J_r(N_L + \boldsymbol{j} f_{fL})]e^{\boldsymbol{j}\gamma} \end{aligned} \tag{35}$$

For the stator, Eq.(12) becomes

$$\begin{bmatrix} J_{s11} & J_{s} \\ J_{s} & J_{s22} \end{bmatrix} \begin{Bmatrix} \ddot{\boldsymbol{r}}_{\boldsymbol{rL}} \\ \ddot{\boldsymbol{r}}_{\boldsymbol{rR}} \end{Bmatrix} + \begin{bmatrix} c_{sL} & 0 \\ 0 & c_{sR} \end{bmatrix} \begin{Bmatrix} \dot{\boldsymbol{r}}_{\boldsymbol{rL}} \\ \dot{\boldsymbol{r}}_{\boldsymbol{rR}} \end{Bmatrix} + \begin{bmatrix} K_{sL} & 0 \\ 0 & K_{sR} \end{bmatrix} \begin{Bmatrix} \boldsymbol{r}_{\boldsymbol{rL}} \\ \boldsymbol{r}_{\boldsymbol{rR}} \end{Bmatrix} = \begin{Bmatrix} N_L + \boldsymbol{j} f_{fL} \\ -(N_R + \boldsymbol{j} f_{fR}) \end{Bmatrix} \tag{36}$$

For the assumed solution

$$\begin{aligned} \boldsymbol{r}_{\boldsymbol{rL}} &= r_{rL0} e^{\boldsymbol{j}(\gamma_0 - \Omega t)} \quad , \quad \boldsymbol{r}_{\boldsymbol{sL}} = r_{sL0} e^{\boldsymbol{j}(\gamma_0 - \Omega t)} \\ \boldsymbol{r}_{\boldsymbol{rR}} &= r_{rR0} e^{\boldsymbol{j}(\gamma_0 - \Omega t)} \quad , \quad \boldsymbol{r}_{\boldsymbol{sR}} = r_{sR0} e^{\boldsymbol{j}(\gamma_0 - \Omega t)} \end{aligned} \tag{37}$$

The steady-state solutions are:

$$\begin{aligned} \boldsymbol{r}_{\boldsymbol{rR0}} &= -\frac{l^2}{I_g m_r \Omega^2} [J_{r11}(N_R + \boldsymbol{j} f_{fR}) + J_r (N_L + \boldsymbol{j} f_{fL})] \\ \boldsymbol{r}_{\boldsymbol{rL0}} &= \frac{l^2}{I_g m_r \Omega^2} [J_{r22}(N_L + \boldsymbol{j} f_{fL}) + J_r (N_R + \boldsymbol{j} f_{fR})] \\ \boldsymbol{r}_{\boldsymbol{sL0}} &= \frac{(N_L + \boldsymbol{j} f_{fL}) Z_{sR} - (N_R + \boldsymbol{j} f_{fR}) J_{s12} \Omega^2}{\boldsymbol{A}} \\ \boldsymbol{r}_{\boldsymbol{sR0}} &= \frac{-(N_R + \boldsymbol{j} f_{fR}) Z_{sR} + (N_L + \boldsymbol{j} f_{fL}) J_{s12} \Omega^2}{\boldsymbol{A}} \end{aligned} \tag{38}$$

The constraint Eq.(13), become

$$\begin{aligned} C_{rR} &= \boldsymbol{r}_{\boldsymbol{rR0}} - \boldsymbol{r}_{\boldsymbol{sR0}} \\ -C_{rL} &= \boldsymbol{r}_{\boldsymbol{rL0}} - \boldsymbol{r}_{\boldsymbol{sL0}} \end{aligned} \tag{39}$$

Substituting $\boldsymbol{r_{rL0}}, \boldsymbol{r_{rR0}}, \boldsymbol{r_{sL0}}, \boldsymbol{r_{sR0}}$ from Eq.(38) into Eq.(39) gives

$$C_{rL} = (N_L + \boldsymbol{j}f_{fL})[\frac{J_{r22}l^2}{I_g m_r \Omega^2} - \frac{\boldsymbol{Z_{sR}}}{\boldsymbol{A}}] + (N_R + \boldsymbol{j}f_{fR})[\frac{J_r l^2}{I_g m_r \Omega^2} + \frac{J_s \Omega^2}{\boldsymbol{A}}]$$

$$C_{rR} = (N_L + \boldsymbol{j}f_{fL})[\frac{J_r l^2}{I_g m_r \Omega^2} + \frac{J_s \Omega^2}{\boldsymbol{A}}] + (N_R + \boldsymbol{j}f_{fR})[\frac{J_{r11}l^2}{I_g m_r \Omega^2} - \frac{\boldsymbol{Z_{sL}}}{\boldsymbol{A}}] \tag{40}$$

Equations (36),(37) can be stated

$$\begin{bmatrix} \boldsymbol{W_{11}} & \boldsymbol{W} \\ \boldsymbol{W} & \boldsymbol{W_{22}} \end{bmatrix} \begin{Bmatrix} N_L + \boldsymbol{j}f_{fL} \\ N_R + \boldsymbol{j}f_{fR} \end{Bmatrix} = \begin{bmatrix} C_{rL} \\ C_{rR} \end{bmatrix} \tag{41}$$

Comparing this result to the mode-1 result of Eq. (24) shows a difference in sign for the off-diagonal coefficient matrix entries. The mode-2 solution is:

$$N_L + \boldsymbol{j}f_{fL} = \frac{C_{rL}\boldsymbol{W_{22}} - C_{rR}\boldsymbol{W}}{\boldsymbol{D_w}}$$

$$N_R + \boldsymbol{j}f_{fR} = \frac{C_{rR}\boldsymbol{W_{11}} - C_{rL}\boldsymbol{W}}{\boldsymbol{D_w}} \tag{42}$$

2.5 ANALYTICAL PREDICTIONS FOR MODE 2

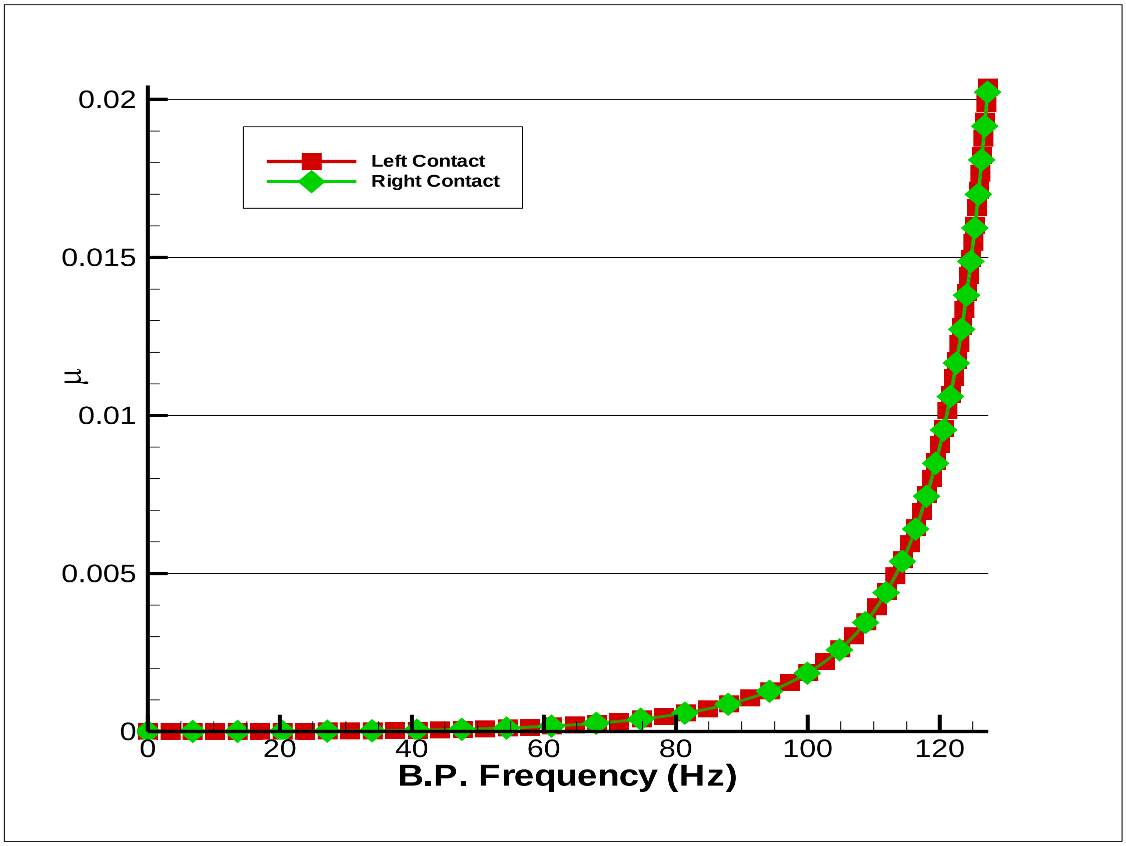

Figure 8 Disk at Center RCl$_L$= RCl$_R$=100. Mode 2

2.5.1 Disk at Center- Mode 2

Since Mode 2 results incorporate the pitch mode frequency the results in Figure 8 are in agreement with the earlier mode 1 results. The whirl region extends from rotor natural frequency (ω_{nr}=0) to pitch mode combined natural frequency (ω_{nc}=135 Hz). Since this frequency is greater than the stator natural frequency, the next whirl region will initiate at higher individual natural frequencies.

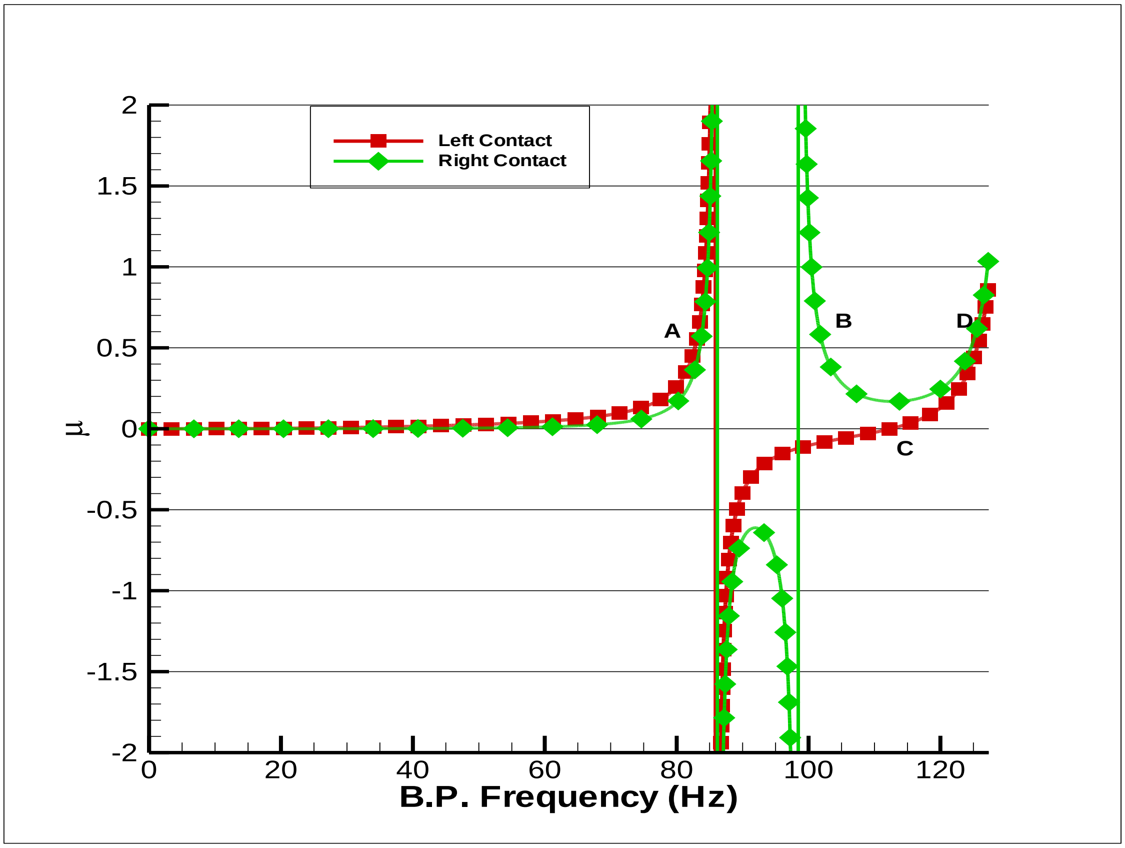

Figure 9 Disk at ¾ Location RCl$_L$= RCl$_R$=100. Mode 2

2.5.2 Disk at ¾ Location- Mode 2

Mode 2, Figure 9 for the disk at ¾ location is very different as compared to mode 2 for the center location, Figure 8. The data (l_g , I_g ,K,c) are same as used in the Mode 1 calculations. The limiting frequency is 87Hz after which it undergoes whirling motion. Beyond this frequency the rotor enters whipping mode. The right contact comes into whirl mode at point B ($\mu_{req} < \mu$) whereas the left contact enters whirl at point C. Since both the contacts have same RCl, we can predict the second whirl mode to start at

C since at this point both the contacts have positive μ and $\mu_{req} < \mu$ .Whip is again expected beyond point D (pitch frequency) since $\mu_{req} > \mu$

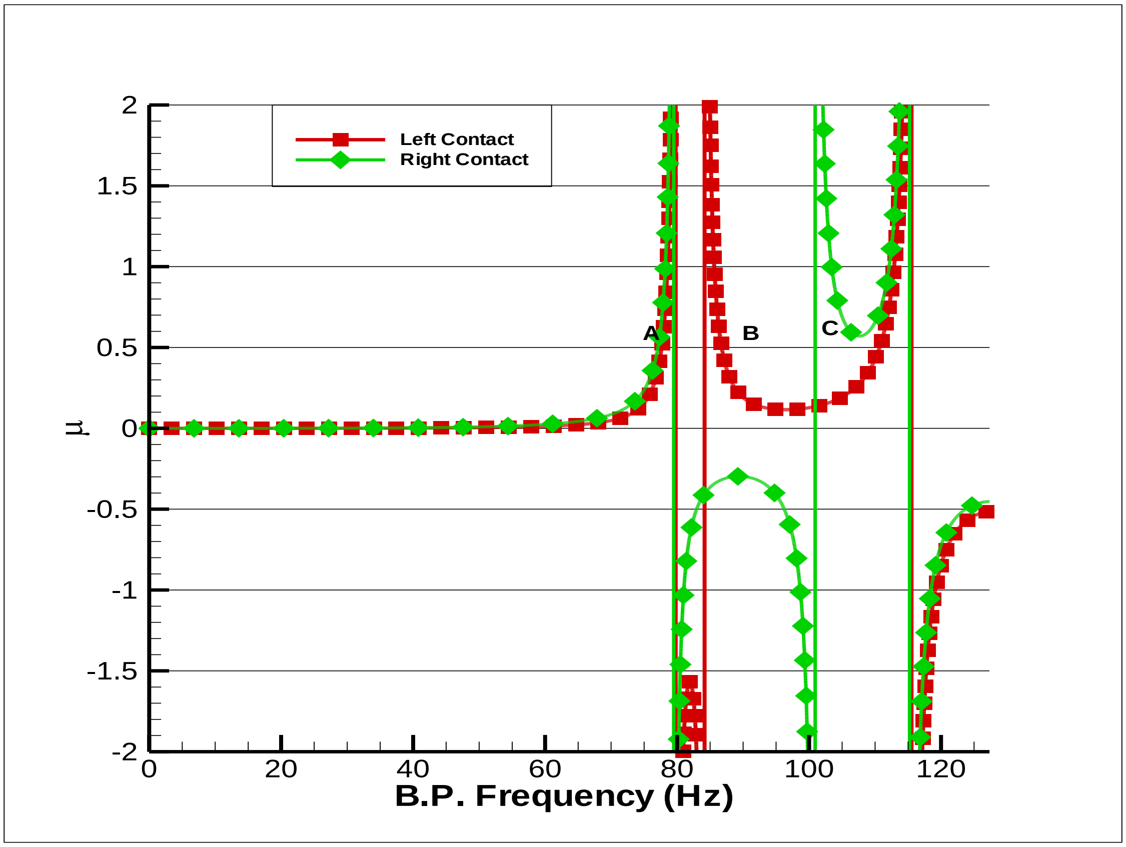

Figure 10 Disk at Overhang Location RCl_L= RCl_R=100. Mode 2

2.5.3 Disk at Overhang Location- Mode 2

For this mode, the data (l_g, I_g, K, c) is same as used for Mode 1 calculations. From Figure 10, whirling is seen at the two contacts until A, a frequency of 79 Hz (compared to rotor stator pinned frequency of 87 Hz) beyond which it transitions to whip. There is no second whirl common to both contacts. The required μ value at point C is greater than .5 for the right contact. Since both the contacts have same RCl, whirling can be predicted only when both contacts seems to be whirling simultaneously which is not seen after the first transition.

CHAPTER III

SIMULATION MODEL

3.1 OVERVIEW OF *XLTRC*^{2} ROTORDYNAMIC SOFTWARE PACKAGE

The simulations were performed using XLTRC^2, a component-mode, finite-element program that uses Timoshenko beam finite elements to generate a rotor and a stator model [19]. The dynamics model consists of physical and modal coordinates, which makes it possible to eliminate higher frequency mode shapes without disturbing physical coordinates at locations of nonlinear connections. For more information on component mode synthesis on XLTRC^2, consult Childs [20] or TAMU Turbomachinery Laboratory *XLTRC*^{2} Brochure [21].

3.2 GENERAL SYSTEM MODEL

The *XLTRC*^{2} simulation model used for this research is shown in Figure 11. The model consists of a rotor shaft with a centrally mounted disk. The model for the rotor is simulated with two rigid rotor shafts connected to the disc on either side. The density of the disk is higher than the rotor to make it heavier. The rotor shaft is divided into 8 finite elements. Similar models are seen in Figures 12 and 13 with the difference in disc positions. The stator is modeled as a heavier mass, hollow shaft and is elastically supported to the ground with linear springs and dampers. The stator is divided into 8 finite elements. Stations 2, 12 and 10, 20 provide no linear support or damping and act only as locations for nonlinear contact. The model in Figure 11 is a flexible analog of the rigid body model in E.g. (31). It has the same properties and mass as in E.g. (31). The subsequent Figures (12) and (13) are flexible analogs corresponding to ¾ disk location and disk at overhang location.

Three different cases are simulated. The rotor and stator have the same constant properties and contact points, but the mass disk is shifted from middle, to a ¾ location, and then further beyond the contact point to an overhang location giving rise to three separate cases.

Table 1 Division of Cases and Subcases for Simulation Model

CASE	SUBCASE	RCl_L	RCl_R
(A) Disk at center	(a)	100	100
(A) Disk at center	(b)	100	125
(B) Disk at ¾ location	(a)	100	100
(B) Disk at ¾ location	(b)	100	125
(B) Disk at ¾ location	(c)	125	100
(C) Disk at overhang location	(a)	100	100
(C) Disk at overhang location	(b)	100	125
(C) Disk at overhang location	(c)	125	100

The Anemometer had small RCl values on the order of 30. To imitate real turbo machinery, RCl values of 100 and 125 were chosen since they are much closer to what is found in real turbo machines. But too high RCl values will create much higher Backward Precessional (BP) frequencies which is not practical. Hence, values of 100 and 125 were chosen for the model.

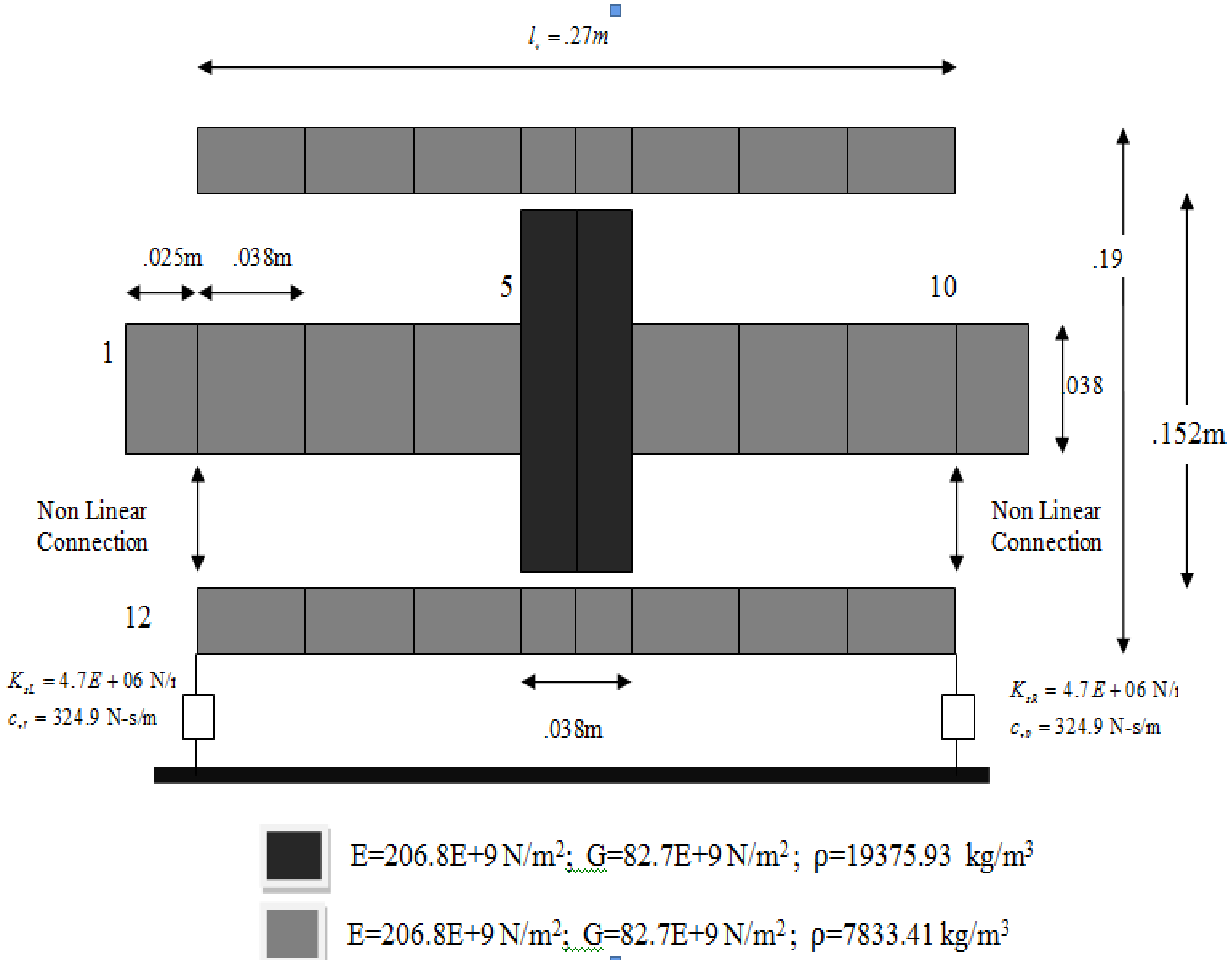

Figure 11 XLTRC^2 Simulation Model (rotor+ stator) for Disk at Center

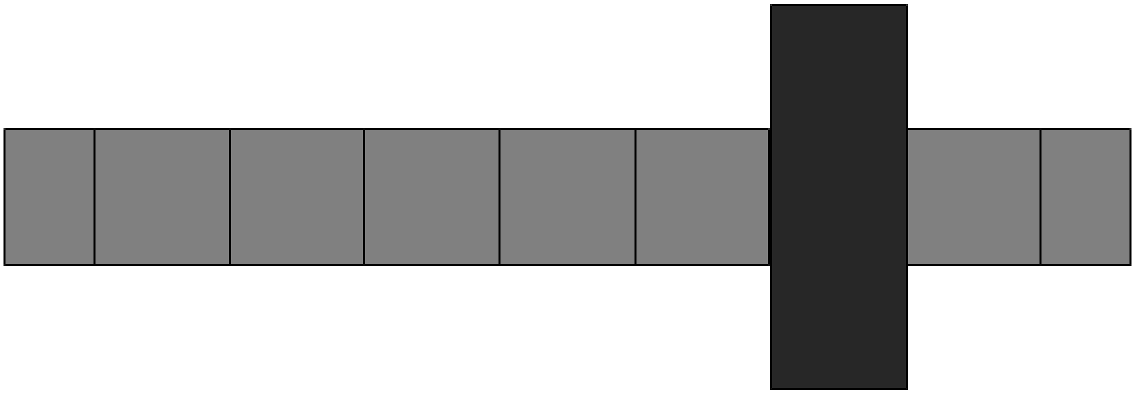

Figure 12 XLTRC^2 Simulation (rotor) for Disk at ¾ Location

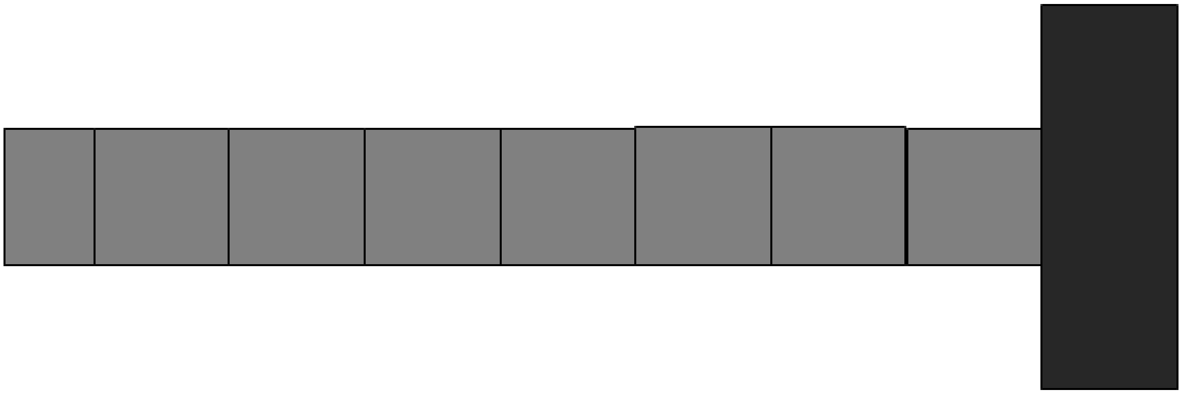

Figure 13 XLTRC^2 Simulation (rotor) for Disk at Overhang Location

Table 1 shows the Frequencies for the rotor and stator pinned together. Table 2 shows the damping ratio and damped natural frequency for the above 3 configurations.

Table 2 Caclulated Rotor-Stator Pinned Natural Frequencies.

	Bounce Frequency (ω_{n1}) (Hz)	Damping Ratio (Zeta1)	Pitch Frequency (ω_{n2}) (Hz)	Damping Ratio (Zeta2)	1st bending mode (ω_{n3}) (Hz)	Damping Ratio (Zeta3)
Disk at center	87.9	.019	133.8	.029	595.1	.009
Disk at ¾ location	86.9	.019	127.9	.028	709.8	.013
Disk at Overhang	82.4	.018	115.4	.025	701.3	.005

The values have been calculated by providing a very stiff bearing ($K_{contact,L}$= $K_{contact,R}$ =4.5E+08 N/m $c_{contact,L}$ = $c_{contact,R}$ =2.1E4 N-s/m) at the rub locations to simulate a pinned rotor stator bearing. During nonlinear simulations the reaction force is zero without contact and is defined by Eq. (43) with contact. Table 3 is for the frequencies related to the elastically supported stator alone.

Table 3 Calculated Stator Natural Frequencies.

	Bounce Frequency (ω_{n1}) (Hz)	Damping Ratio (Zeta1)	Pitch Frequency (ω_{n2}) (Hz)	Damping Ratio (Zeta2)	1st bending mode (ω_{n3}) (Hz)	Damping Ratio (Zeta3)
Stator	105.4	.023	143	.031	8232.9	.000

3.3 NONLINEAR CONNECTION

Nonlinear interaction at the rub location was modeled using a modified form of Hunt's and Crossley's [17] coefficient-of-restitution model. The normal force was given by

$$N = k_{nl,1}\delta + k_{nl,2}\delta^2 + c_{nl}\,\dot{\delta}\,\delta \tag{43}$$

where $k_{nl,1}$, $k_{nl,2}$ and c_{nl} are stiffness and damping coefficients and δ represents the deflection at the rub surface. The transverse friction force is

$$F_F = \mu N \operatorname{sgn}(V_t) \tag{44}$$

where $\operatorname{sgn}(V_t)$ being introduced by Bartha [10] to account for relative transverse contact velocity and V_t is the Relative tangential surface velocity vector at contact given by

$$\boldsymbol{V_t} = \dot{r}_{rX}\boldsymbol{I} + \dot{r}_{rY}\boldsymbol{J} + \boldsymbol{\omega}\times\boldsymbol{R} \tag{45}$$

For the current model, the following stiffness and damping values were used

$$\begin{aligned} k_{n1,1L} &= k_{n1,1R} = 1.75E+11 \text{ N/m} \\ k_{n1,2L} &= k_{n1,2R} = 0 \\ c_{n1,L} &= c_{n1,R} = 1.75E+05 \text{ N-s/m} \end{aligned} \tag{46}$$

E.g. $N = 1.75E + 11 * \delta + 0 * \delta^2 + 1.75E + 05 * \dot{\delta} * \delta$

Hence the contact model is linear. The value of $r_{rL} = r_{rR}$ =38.1mm was used for radius of contact. Further μ=0.5The value of coefficient of friction was taken to be .5. A higher value of μ gave a better chance of exhibiting whip and whirl behavior, to study for analysis. The stiffness and damping coefficient values were obtained by scaling values from Wilkes thesis [22] and further adjusting them to get better responses and results.

3.4 IMBALANCE

An additional imbalance was added on to the disk. An API imbalance was calculated using the empirical formula

$$imbalance(\text{oz-inch}) = \frac{4 * w(lbs)}{N(rpm)} \tag{47}$$

A running speed of 6000 rpm was chosen. This gave an imbalance value of 3.43 gm-cm. The imbalance was only introduced in the CASE A; (a), It did not make any substantial changes to the results and hence was not used in other simulation models.

3.5 SIMULATION PROCEDURE AND POST PROCESSING OF DATA

Whip and whirl behavior was initiated by exciting the shaft with an impulsive force thereby bringing the rotor in contact with the stator. At 20 rpm, this simulation was run until a steady-state cycle persisted, followed by running a new simulation with increased rotor speed from the previous state. The procedure was repeated for increasing rotor speed from 20 rpm to 258rpm. The predictions, recorded for each simulation consisted of the rotor’s position and velocity at each of the contact points relative to the stator’s position. These variables were then extracted by MatLab and converted into frequency domain for analysis. Relative contact point-velocities were analyzed to determine the presence of either pure sliding or rolling with slipping.

A similar procedure was used for analyzing the whip and whirl behavior when speeds are decreased. The motion is initiated by exciting the shaft with an impulsive force thereby bringing the rotor in contact with the stator. At 252 rpm, this simulation was run until a steady state persisted, followed by running a new simulation with decreased rotor speed from the previous state. The procedure was repeated for decreasing rotor speed from 252 rpm to 20 rpm.

3.6 METHOD OF COMPARISON

Direct comparison between analytical and simulation model for whip and whirl regimes is not possible due to the different output variables predicted by the two models. The analytical solution predicts required μ values versus corresponding BP frequencies. The simulation generates predictions of BP frequency against rotor running speed. By definition when μ_{req} exceeds μ, whipping occurs and jumps back to whirling when $\mu_{req} < \mu$. Thus whirling and whipping are predicted.

The simulation prediction provides plot of BP frequencies versus ω. Hence, untill the rotor is not slipping, BP frequency increases with increasing running speed, thus observing a whirl regime. When the rotor starts slipping, the BP frequency will remain constant with increasing rotor speed indicating whipping regime. Thus, indirectly, the whirl and whip ranges predicted from the above two methods of analytical solution and nonlinear simulation are compared.

3.7 SIMULATED STATOR SUPPORT CONFIGURATION

The stator was supported elastically. The support stiffness and damping used at the two ends of the stator are given below.

$$\begin{aligned} K_{sL} &= K_{sR} = 4.7E+6 \text{ N/m} \\ c_{sL} &= c_{sR} = 324.9 \text{ N-s/m} \end{aligned} \tag{48}$$

These are the same values that were used in the analytical model. Referring to Childs and Bhattacharya [12], the system was chosen to be lightly damped to obtain results. Also, a viscous damper is used at the center location between rotor and stator, which is very lightly damped. This damper attenuates shock created by the initial impulsive excitation. The value used for this damping is $c= 52$ N-s/m.

CHAPTER IV

NONLINEAR SIMULATION PREDICTIONS

Analytical and Simulation predictions are compared in this chapter. Analytical predictions were presented in Chapter 2 and analyzed for the whirl and whip regimes. Now simulation predictions will be presented for comparison to the analytical prediction.

4.1 SIMULATION VALIDATION

How well will analytical predictions agree with the simulated whip and whirl behavior? Due to computing time constraints each rotor speed simulation was run for 1.5 seconds. This gave a frequency resolution of .67 Hz. Also, since the Runge Kutta method was used for the simulations, for each simulation there were multiple prediction values when calculating the velocity at contact, thus an average of these values was chosen for that corresponding simulation.

4.2 WHIP AND WHIRL FREQUENCIES

4.2.1 Case A- The Disk at Center

Subcase (a) $RCl_L= RCl_R=100$

This case is symmetric. The comparison between the analytical and simulation predictions is provided by comparing the main-component BP frequency versus the rotor running speed as shown in Figure 14(a). The whirl region extends to 56 rpm (BP frequency increasing with increasing rotor speed) beyond which it enters the whipping mode (BP frequency stays constant with increasing rotor speed). The rotor continues whipping at a frequency of 84.6 Hz which extends until a rotor running speed of 160rpm beyond which it again jumps to a whirling solution. As shown in Figure 5 the analytical model predicts a similar behavior for the jump from whirl to whip mode. The required value of friction increases to a value of .5 at 84.5Hz where it is predicted to transition from whirl to whip since $\mu_{req} > \mu$.

To investigate the nature of counter whirl occurring at the contact locations separately, the simulation predictions were analyzed to calculate the speed at the rotor stator contact points given by Eq. (44). Figure 14(b) and 14(c) shows the left and right contact point velocities versus rotor speed, respectively. These results agree with Figure 14(a). For the initial whirling range up to 56 rpm, the contact velocity stays zero, (rolling without slipping condition) followed by a continuous increment in contact velocity until it enters the second whirl region at 160 rpm, and the contact velocity goes back to zero.

Figure 14(d) shows a two sided FFT waterfall plot for the simulation. The whirl frequencies are dominant in the negative frequency region showing backward precession. Harmonic sidebands are present during the whip regions due to the presence of partial rub and contact loss at the contact surfaces. This was confirmed by plotting the simulation predictions in the *XY* plane

Figure 14(e) is the two sided FFT plot produced when an API imbalance or 3.4 gm-cm was introduced on to the disk. No 1X response can be observed in the forward frequency region. The probable reason for its absence is the low speeds at which the simulation is run; there is not enough imbalance excitation to generate an observable 1X component. The only change seen is the reduction in amplitude of the BP frequency. Since there are no changes in any whip or whirl transitions, imbalance was not introduced in any other simulation.

Figure 14(f) show the whirl and whip regimes obtained when simulations were run for decreasing rotor speed. This plot shows the tendency of the rotor to stay in whirl longer before jumping to the whipping mode. These predictions of the rotor's tendency to stay in whirl for a larger period of time are not uncommon in nonlinear models. The same characteristics have been seen before in Wilkes et al. [14] test results.

The above results were for a mode 1 excitation of the rotor. Attempts were made to excite mode2 in the following two ways-

(1) By hitting the ends with impulses in opposite directions

(2) Providing an impulsive moment at the center

Neither method was able to produce a mode2 motion. The disturbed motion would eventually become mode 1 and give the same results as above.

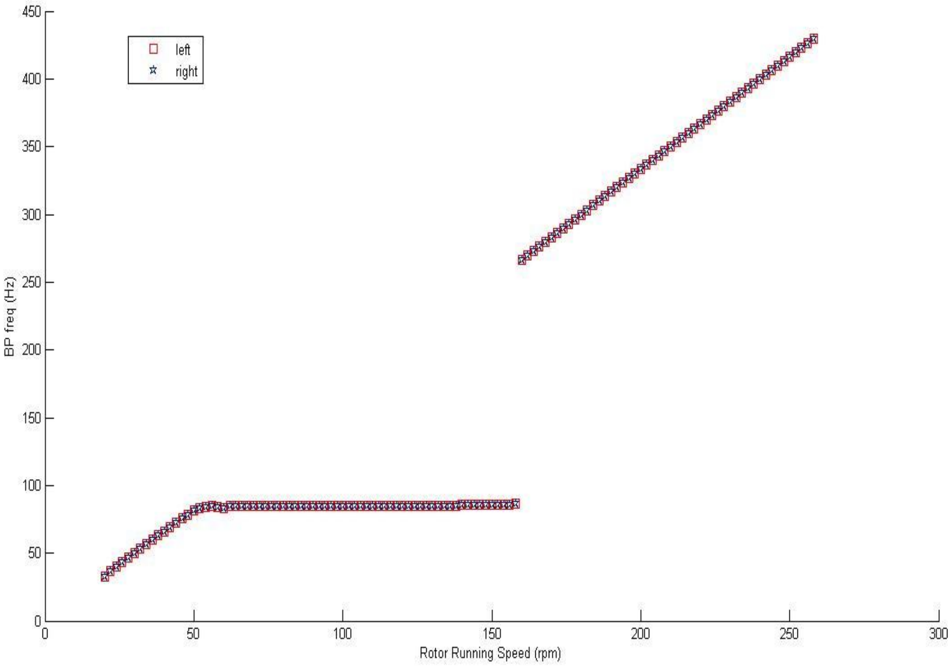

(a) Simulation Results (BP vs Increasing Rotor speed)

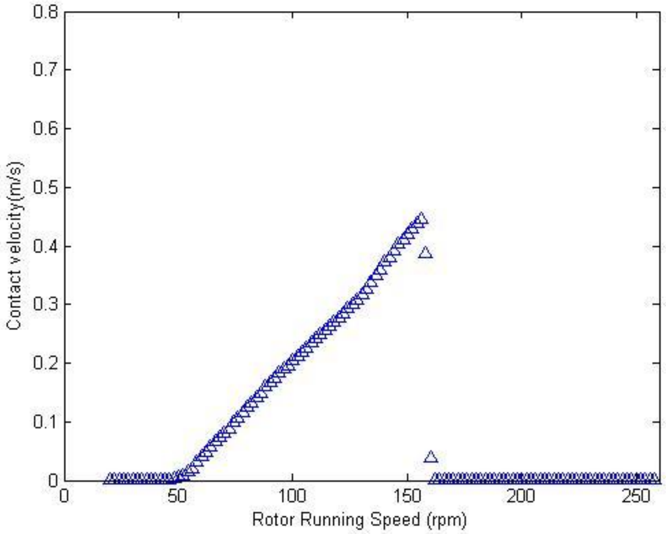

(b) Left Contact Velocity vs Rotor Speed

Figure 14 Disk at Center $RCl_L=RCl_R=100$

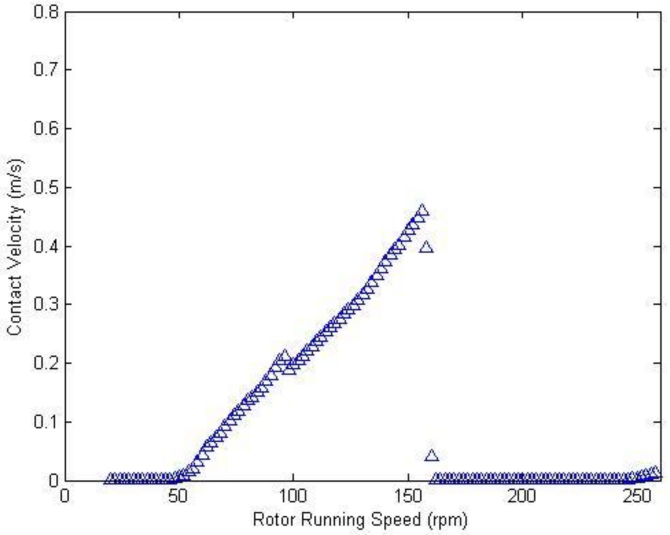

(c) Right Contact Velocity vs Rotor Speed

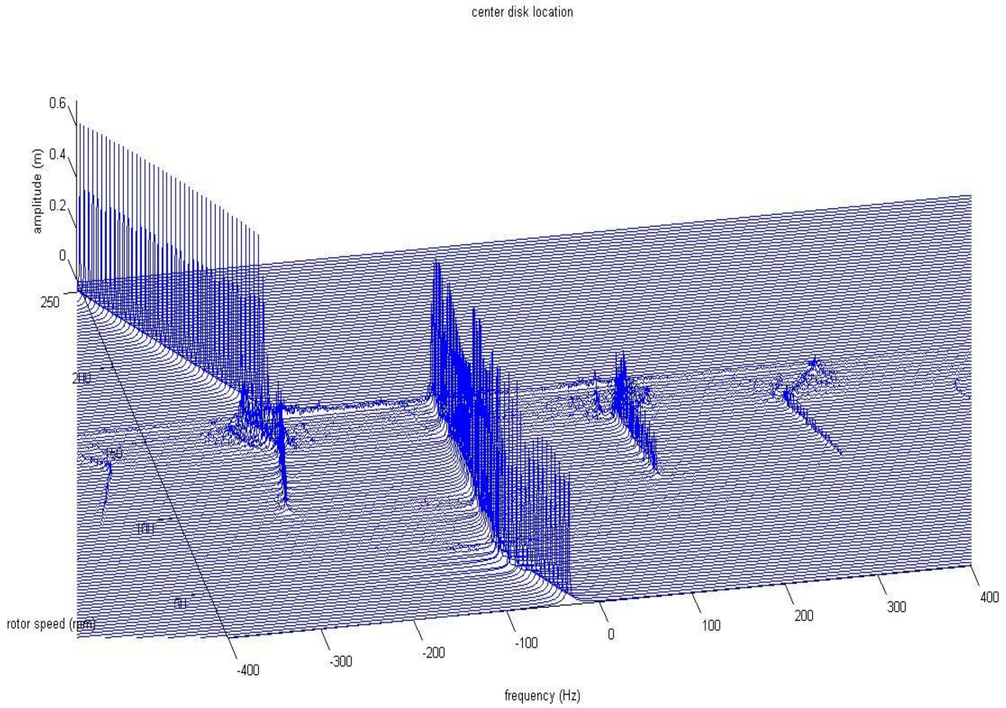
center disk location

(d) Two Sided FFT (Increasing Rotor Speed)

Figure 14 continued

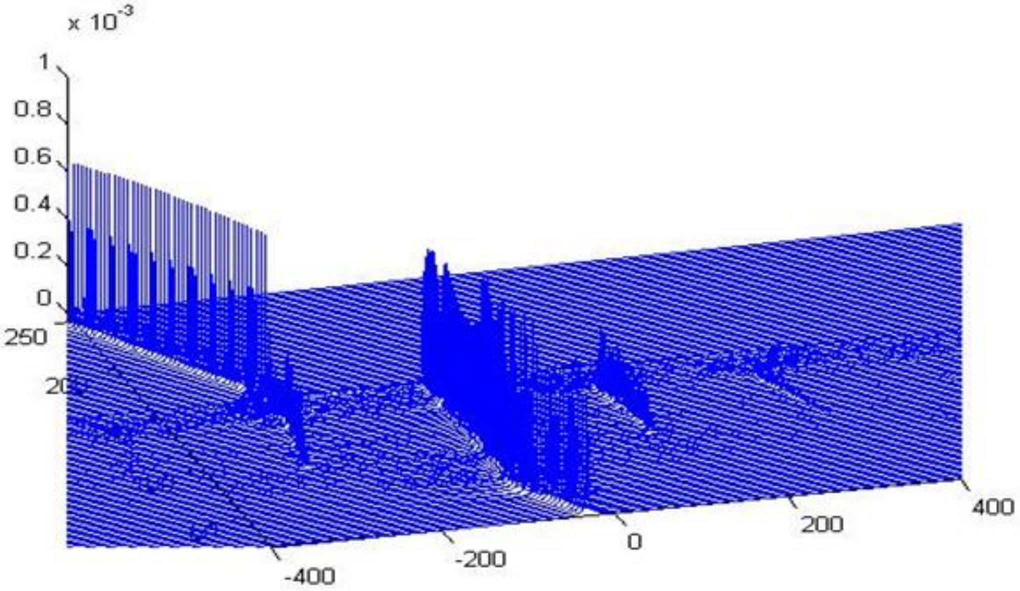

(e) Two Sided FFT (Increasing Rotor Speed with Imbalance)

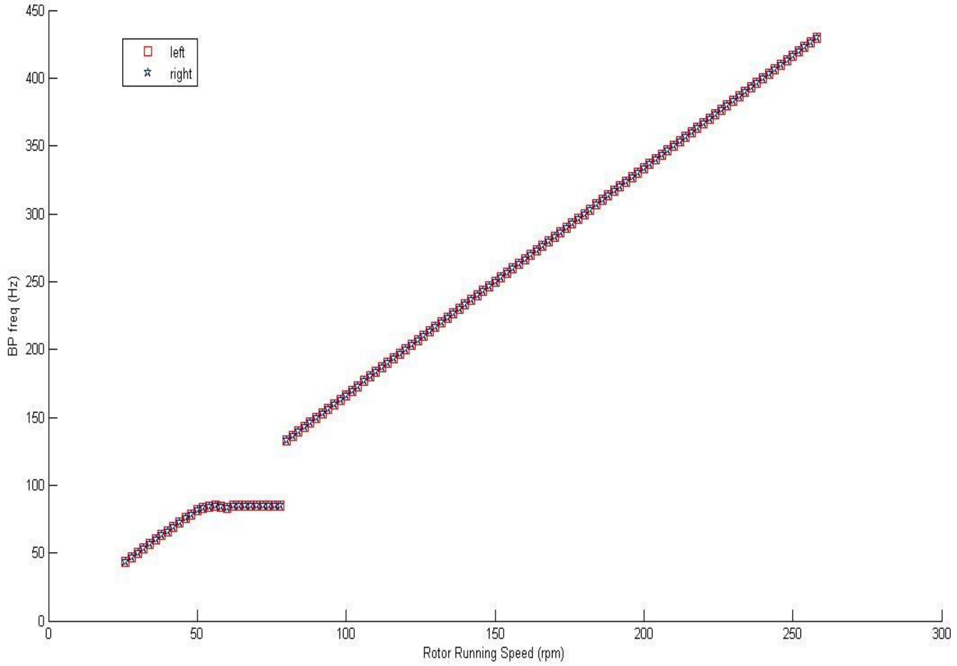

(f) Simulation Results (BP vs Decreasing Rotor Speed)

Figure 14 continued

Subcase (b)-RCl_L=100, RCl_R=125

Since the RCl is different, the analytical solution does not necessarily apply. The simulation for these cases gives interesting, predictions. Figure 15 is a plot of precessional frequency versus ω. Figure 15(a), shows similar characteristics of whirling, transition to whipping 84.6 Hz followed by a jump to the next whirl range.

These results are however misleading suggesting that both contact points are undergoing whirling and whipping simultaneously, which is not possible since they have different RCl values.

When studied individually Figure 15(b) and 15(c) show that both the contact points are slipping continuously. The left contact location, RCl=100 has a lower contact velocity than the right contact location , RCl=125. During the whipping modes the left contact velocity tends to be around zero. The net result is that the backward precession frequency increases with increasing rotor speed thereby *imitating* whirl.

Figure 15(d) shows a two sided FFT plot for increasing rotor speed predictions. Harmonic sidebands are observed during the whipping regions which are attributed to partial rub or lost contact.

Figure 15(e) shows the counter whirling regimes for decreasing rotor speed and as for the case below it shows the tendency to stay in whirl for a longer period as compared to the earlier case of increasing rotor speeds. This behavior is not uncommon in nonlinear models.

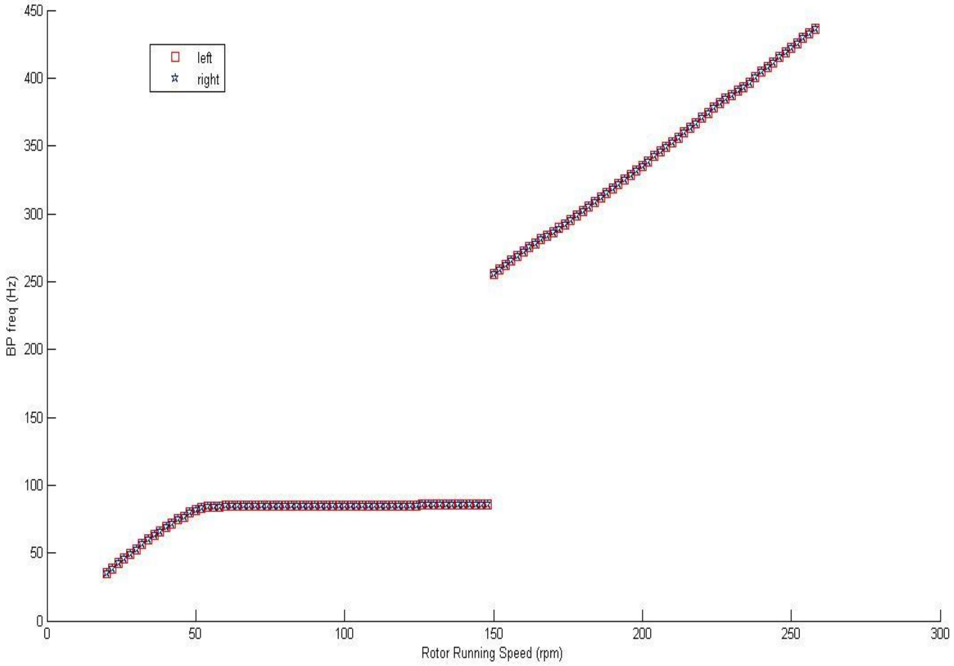

(a) Simulation Results (BP vs Increasing Rotor Speed)

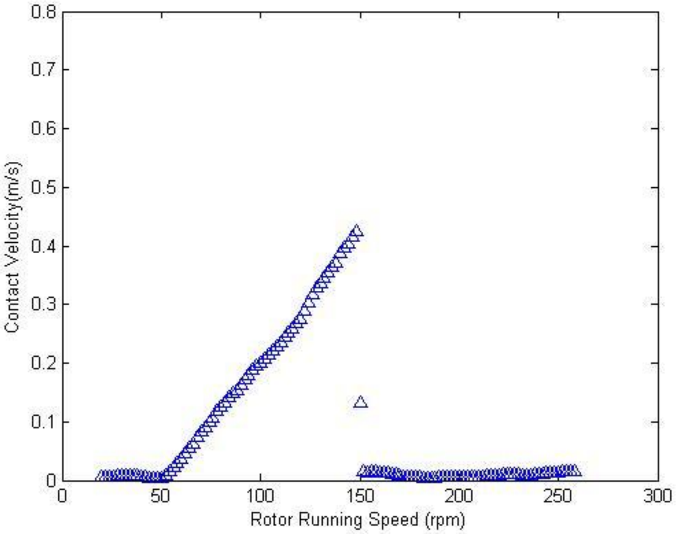

(b) **Left Contact Velocity vs Rotor Speed**

Figure 15 Disk at RCl$_L$= 100, RCl$_R$=125

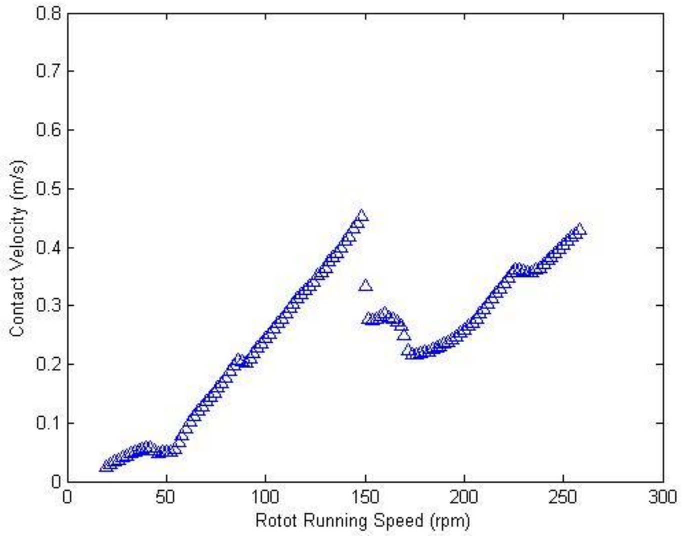

(c) Right Contact Velocity vs Rotor Speed

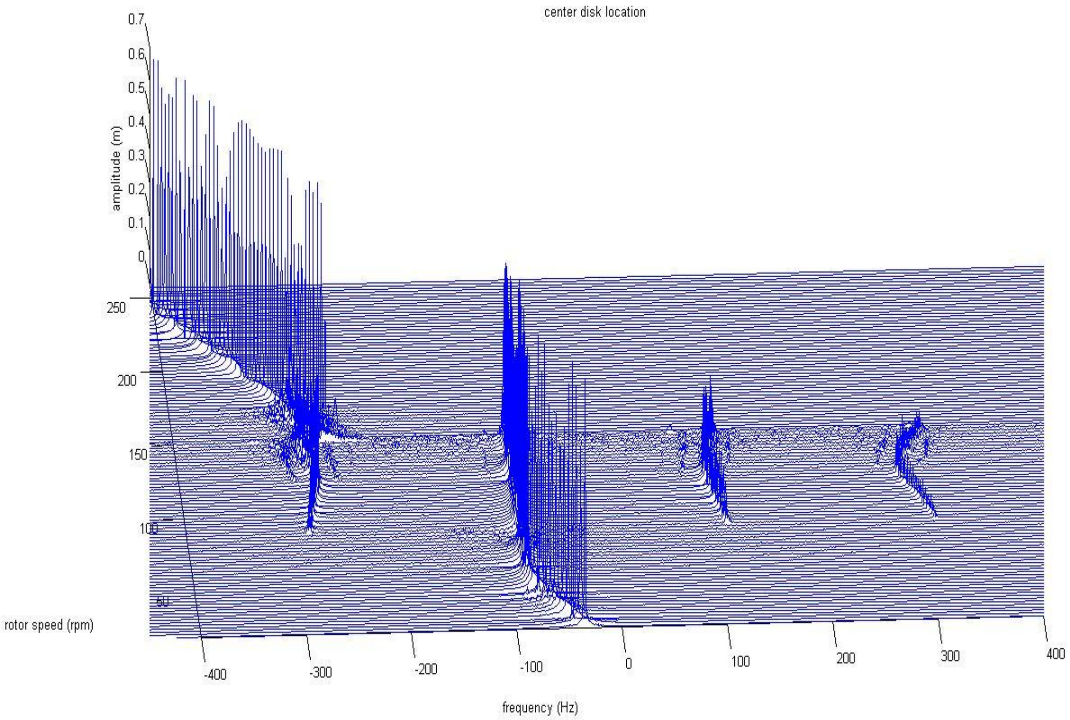

(d) Two Sided FFT (Increasing Rotor Speed)

Figure 15 Continued

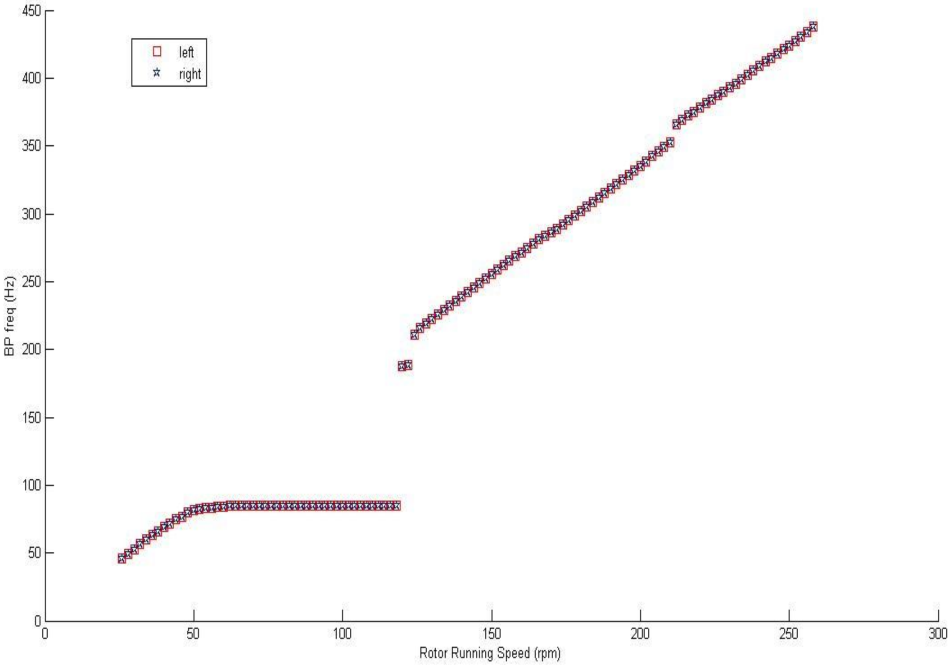

(e) Simulation Results (BP vs Decreasing Rotor Speed)

Figure 15 Continued

4.2.2 Case B- The Disk at ¾ Location

Subcase (a)- $RCl_L = RCl_R = 100$

The disk has been moved to the ¾ location. The analytical predictions in Figure 6 predict whipping to start at 82.6 Hz. The simulation agrees with these predictions in Figure 16(a). The transition to whip occurs at ω=56 rpm where it whips at 82.6 HZ. The whipping frequency slightly increases to 83Hz and then 84.66 Hz. This discrepancy can be attributed to the simulation procedure. The transition from one rotor speed is not continuous but happens in the form of 2 rpm jumps. These jumps might excite the nearby sidebands thus changing the dominant frequency.

The results from the individual contact locations, Figure 16(b) and 16(c) agree with the precessional frequency graph. Both the contact points whirl till 56 rpm, transition to whip, and then transition back to whirl at the same rotor speeds as seen in plot for BP against Rotor speed.

Figure 16 (d) shows the two sided FFT plot again showing multiple sidebands during the whip regime. The negative dominant frequency is for the backward precessional frequency.

Figure 16(e) is a plot of BP frequency versus decreasing rotor speed. It shows a longer range for the whirl regime during deceleration. Being a nonlinear situation such results are always a possibility. Wilkes [22] had similar results in his tests.

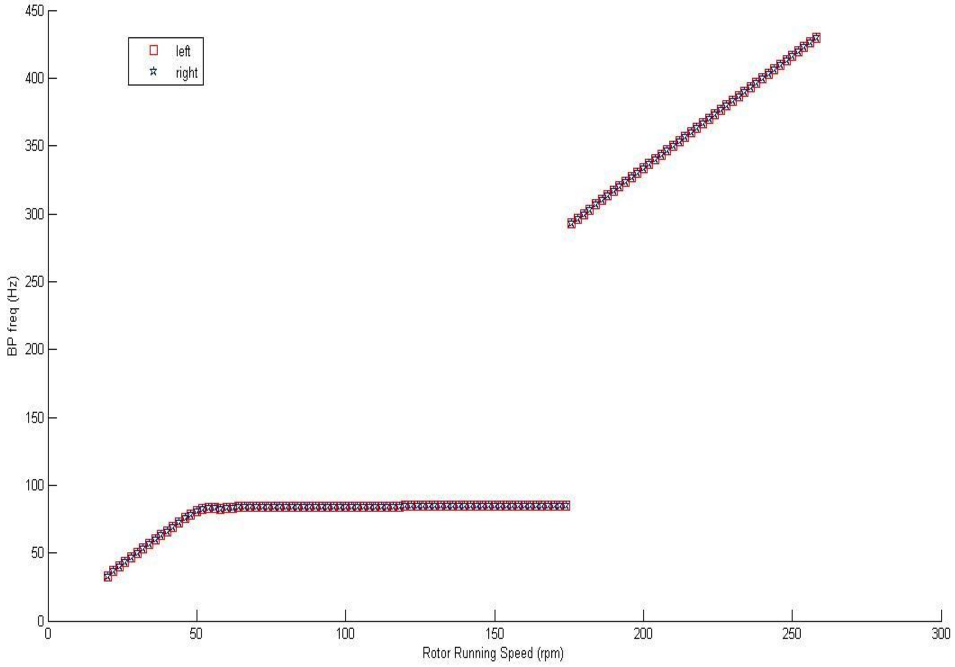

(a) Simulation Results (BP vs Increasing Rotor Speed)

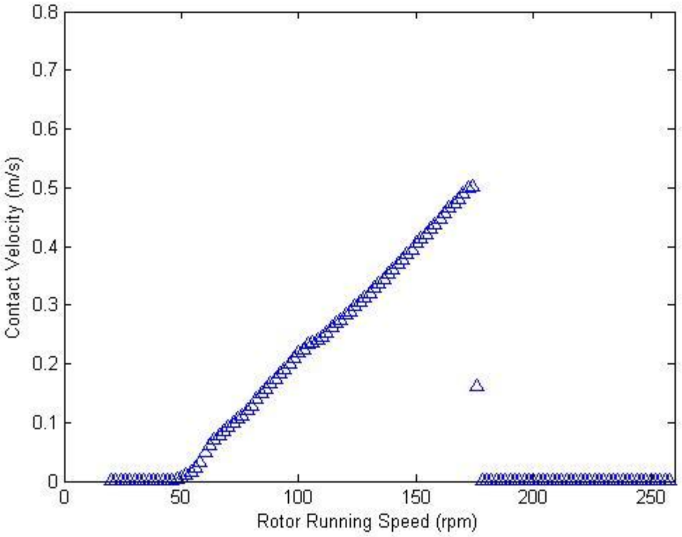

(b) Left Contact Velocity vs Rotor Speed

Figure 16 Disk at ¾ Location RCl$_L$= RCl$_R$=100

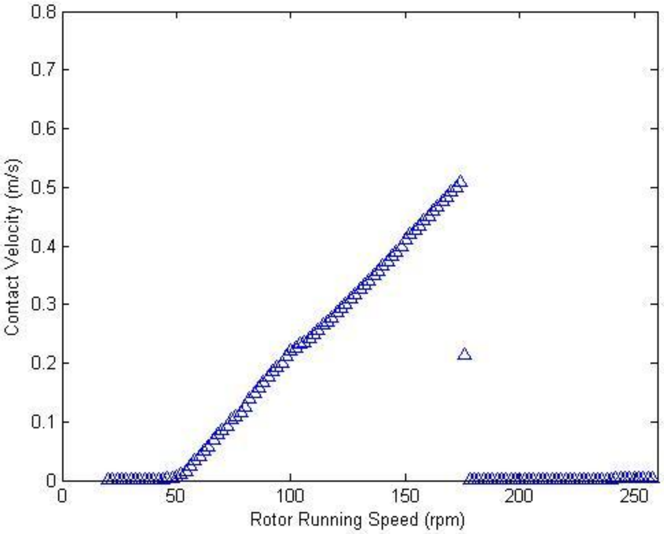

(c) Right Contact Velocity vs Rotor Speed

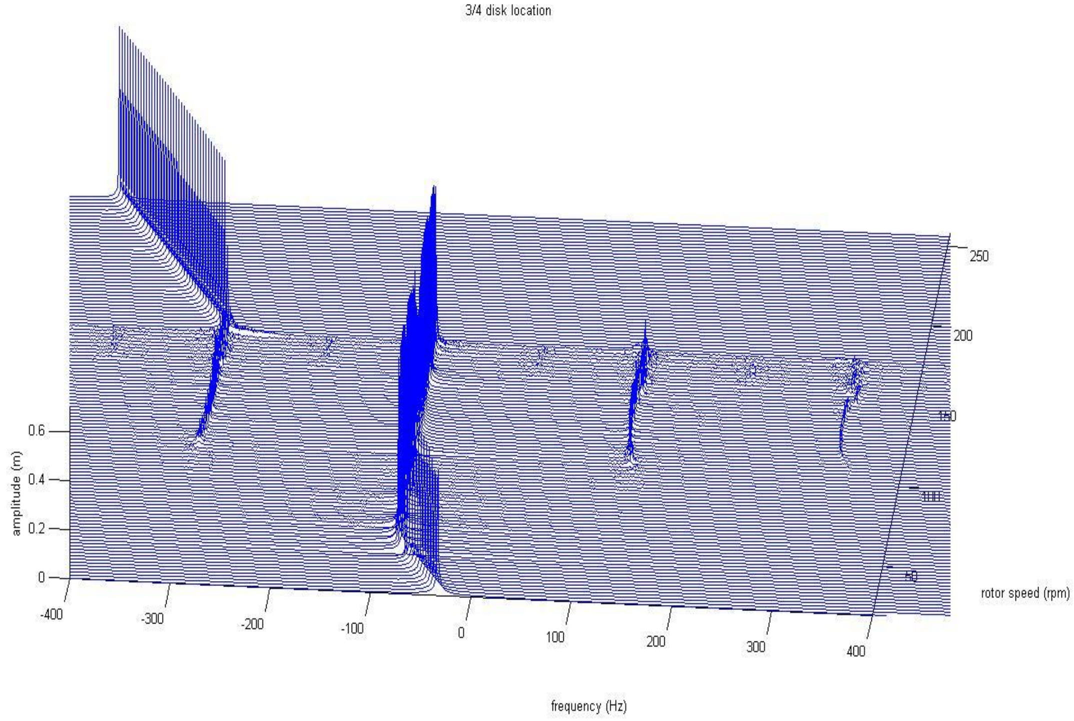

(d) Two Sided FFT (Increasing Rotor Speed)

Figure 16 Continued

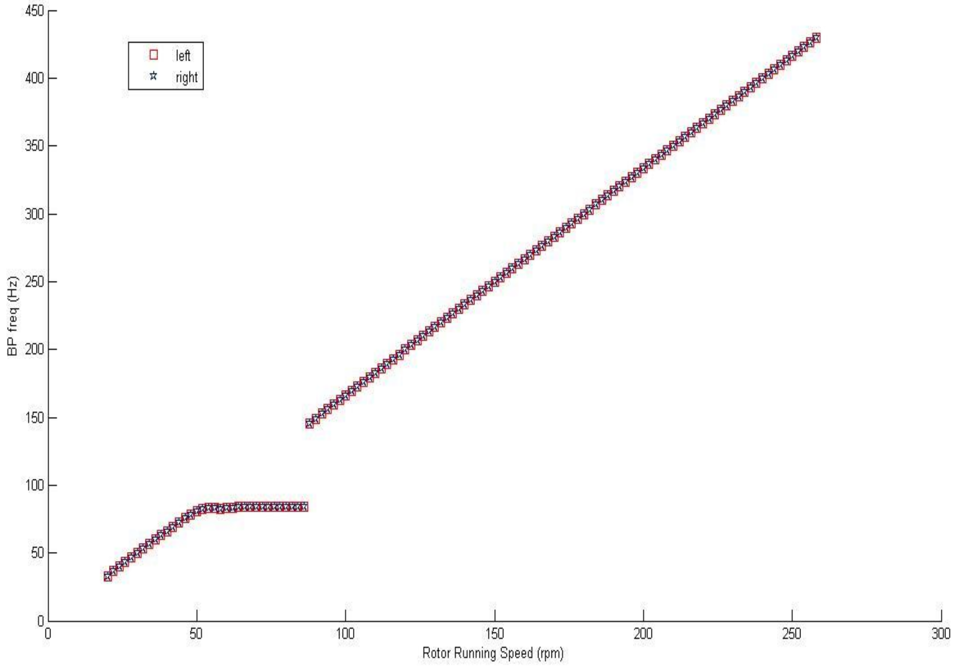

(e) Simulation Results (BP vs Decreasing Rotor Speed)

Figure 16 Continued

Subcase (b)- RCl_L=100, RCl_R=125

Figure 17(a) has the same nominal backward frequency characteristics as for subcase (a), Figure 16(a) (except the second jump frequencies which differ). The transition from whirl to whip occurs at $\omega = 56$ rpm where it whips at 84.66 Hz, stays in this mode until a running speed of 160 rpm when it jumps to the next whirl regime.

Analysis of individual contact points Figure 17(b) and 17(c) show that both points are whipping but one slips more than the other. The velocities drop at transition from whirl to whip but they never drop to zero. Thus, though perceived as whirling, both contacts are whipping at all times. In this case, the Right contact with the RCl=125 is slipping more than the left contact RCl=100. Velocity drop is observed at both the transition running speeds (56 rpm and 160 rpm).

Figure 17(d) is the two sided FFT for the speed up case. As in earlier cases, whipping is accompanied with sideband frequencies possibly due to lost contact or partial rub.

Figure 17(e) plots the BP frequency against rotor speed for decreasing rotor speed. As seen in earlier cases this case shows a similar tendency to stay in the whirl regime for a longer duration as compared to results of increasing rotor speed.

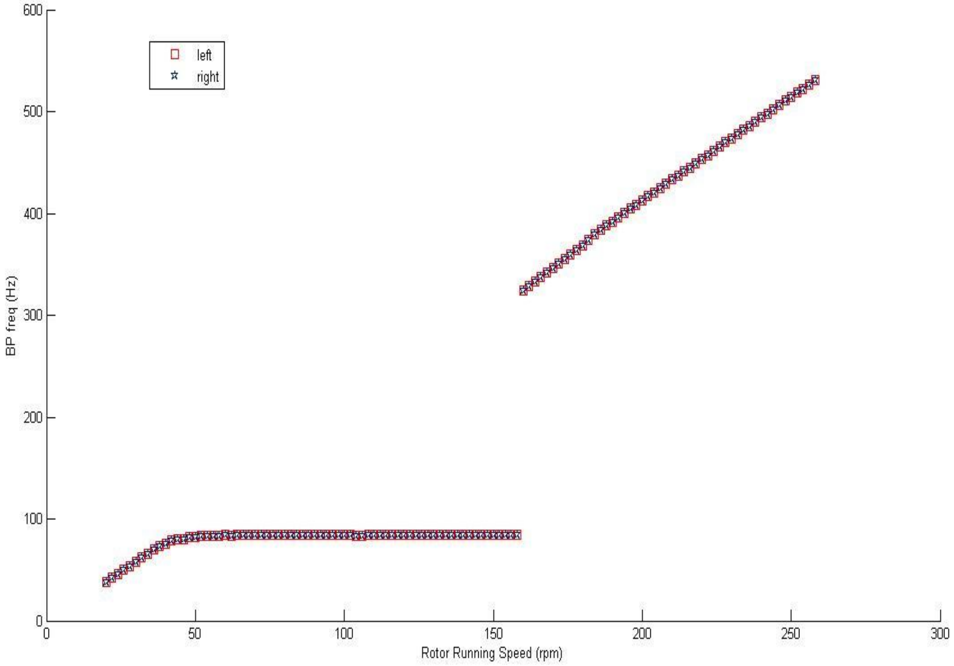

(a) Simulation Results (BP vs Increasing Rotor Speed)

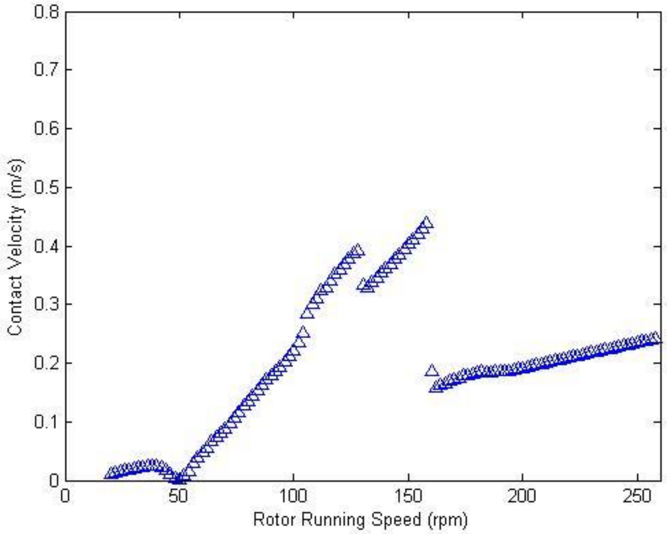

(b) Left Contact Velocity vs Rotor Speed

Figure 17 Disk at ¾ Location RCl_L= 100, RCl_R=125

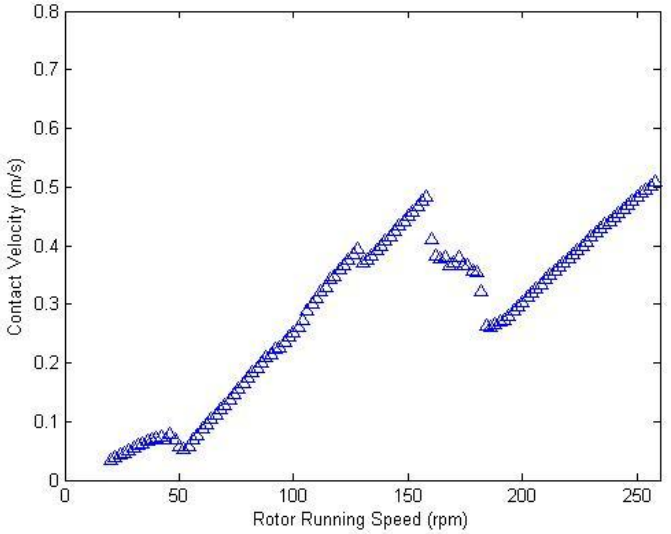

(c) Right Contact Velocity vs Rotor

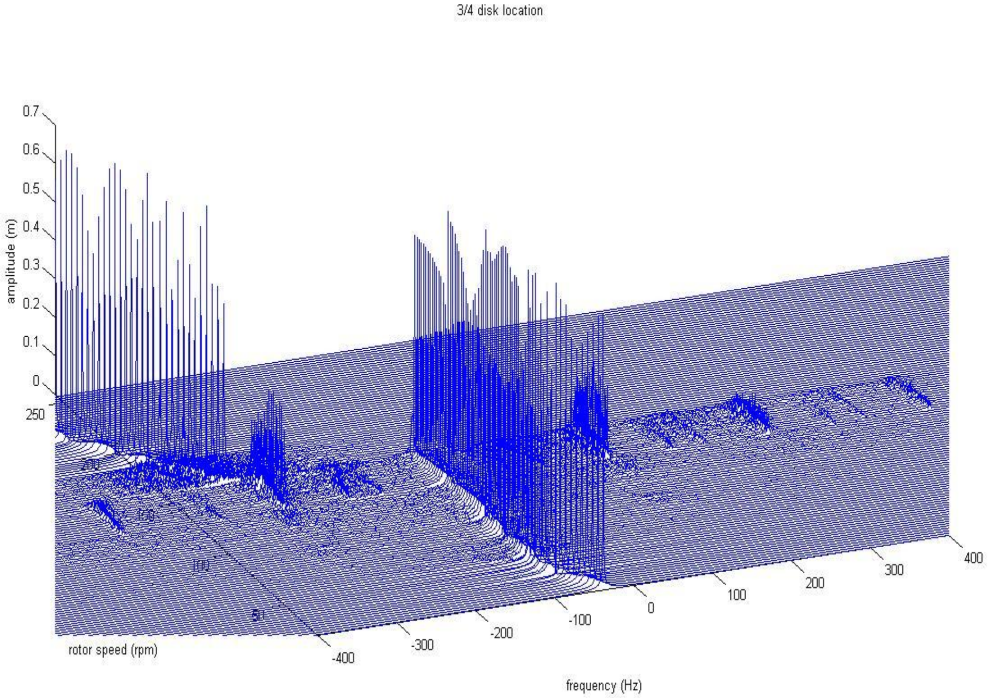

(d) Two Sided FFT (Increasing Rotor Speed)

Figure 17 Continued

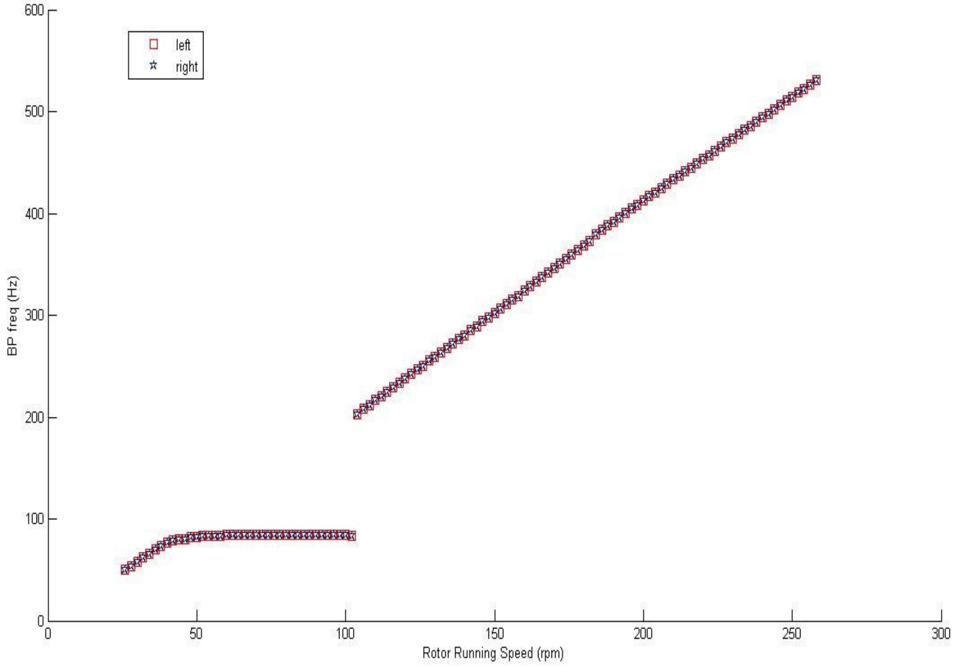

(e) Simulation Results (BP vs Decreasing Rotor Speed)

Figure 17 Continued

Subcase (c)-RCl_L=125, RCl_R=100

Figure 18(a) has the same BP frequency characteristics as for the subcase (a) and (b) as shown in Figure 16(a), 17(a) (except second jump frequency which differs). The transition from whirl to whip occurs at ω=of 56 rpm where it whips at 84.66 Hz. Continues whipping until ω=174 rpm when it jumps to the next whirl regime. This subcase where the disk is closer to end with RCl=100 shows a tendency to stay in whip regime for a longer period as compared to subcase (b).

For an analysis of the contact points, Figure 18(b) and 18(c) show that neither of the points are whirling but instead one of them slips more than the other. The velocities drop at transition from whirl to whip but never drop to zero. Thus though perceived as whirling, both contacts are whipping at all times. In this case, the right contact with the RCl=100 is slipping more than the left contact RCl=125. Thus subcase (b) and (c) show a tendency of more slipping for the contact closer to the disk. Another thing that is observed is, although slipping is continuous, there is always a drop in contact velocity at whirl-to-whip and whip-to-whirl transition running speeds.

Figure 18(d) is the two sided FFT for the speed up case. As with earlier cases, whipping is accompanied with sideband frequencies due to partial rub. The second whirl regime in this case also shows sidebands

Figure 18(e) plots the BP frequency versus ω for decreasing ω. As seen in earlier cases this case shows a similar tendency to stay in the whirl regime for a longer duration as compared to results of increasing rotor speed.

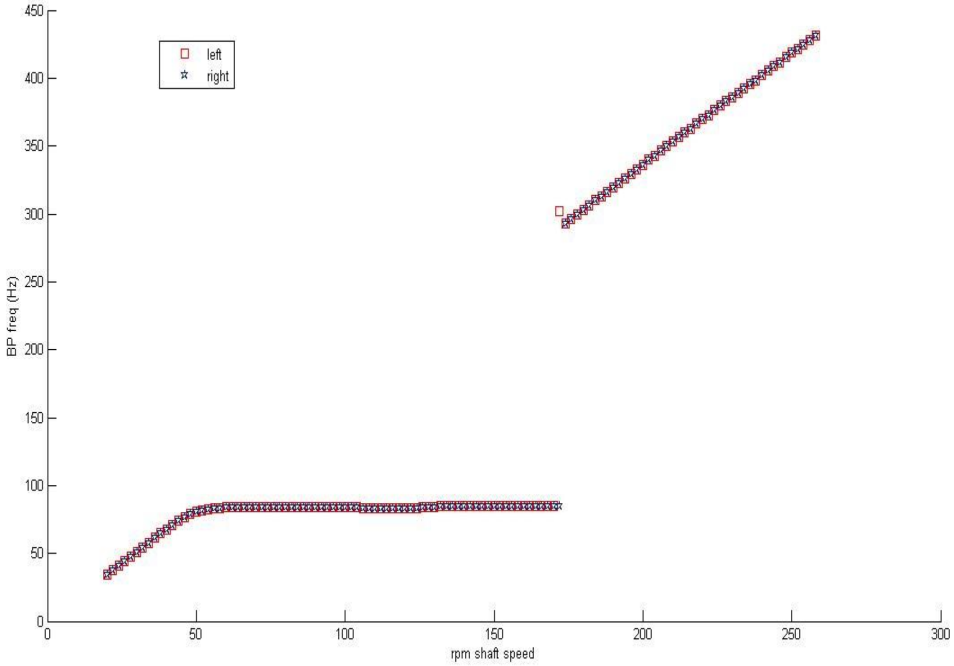

(a) Simulation Results (BP vs Increasing Rotor Speed)

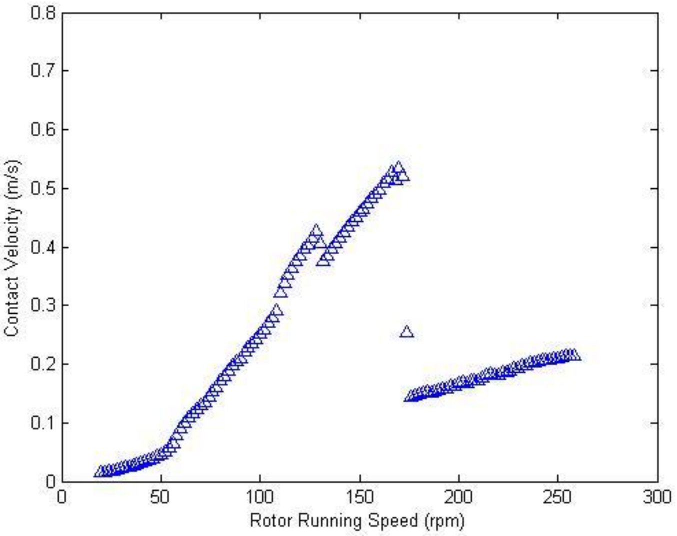

(b) Left Contact Velocity vs Rotor Speed

Figure 18 Disk at ¾ Location RCl_L= 125, RCl_R=100

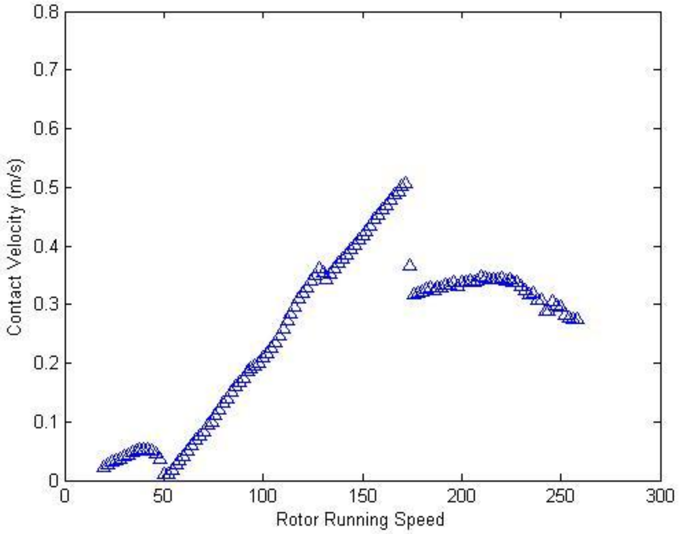

(c) Right Contact Velocity vs Rotor Speed

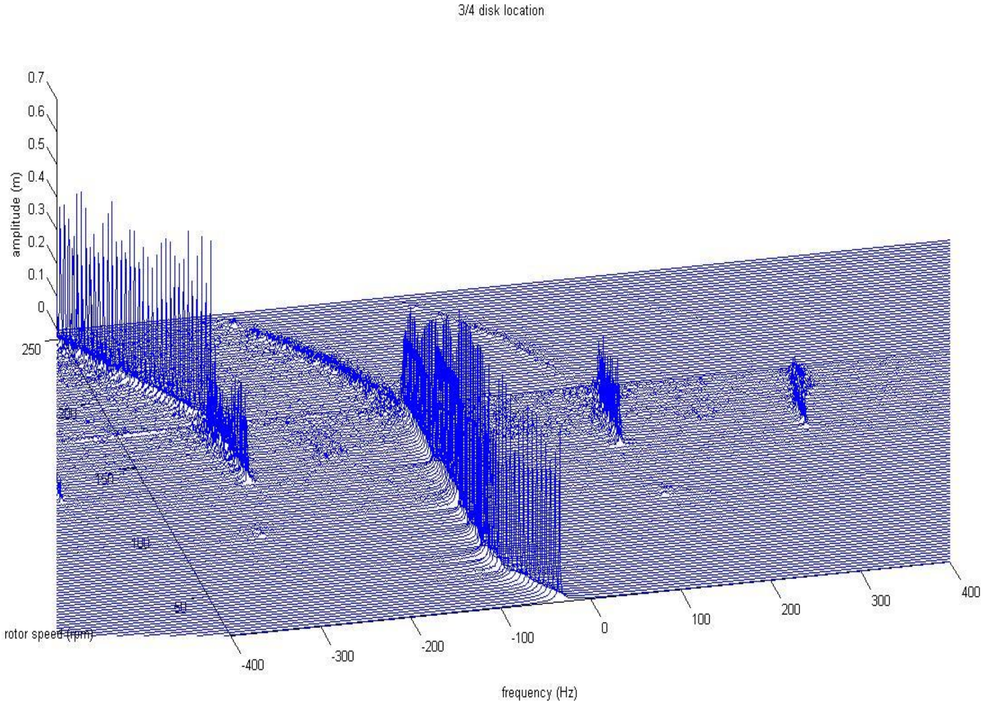

(d) Two Sided FFT (Increasing Rotor Speed)

Figure 18 Continued

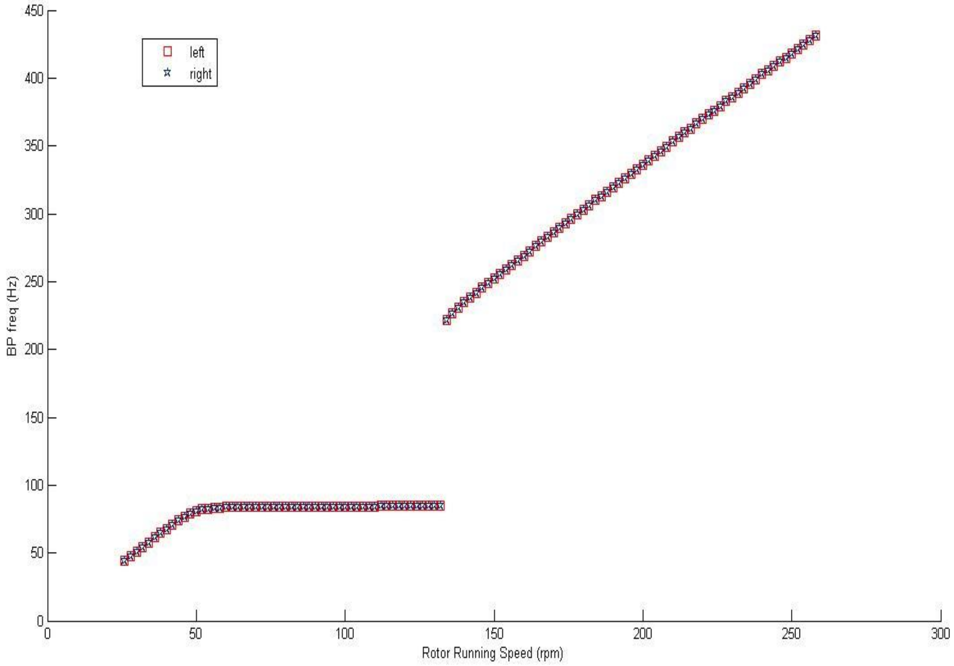

(e) Simulation Results (BP vs Decreasing Rotor Speed)

Figure 18 Continued

4.2.3 Case C- The Disk at Overhang Location

Subcase (a)- $RCl_L=RCl_R=100$

The disk has been moved to a position beyond the right contact location. Figure 19 shows that both the contacts appear to be whirling when they transition to whip at ω=of 56 rpm, continue whipping until 62 rpm and then separately whip at two different frequencies. Neither Mode1nor Mode2 analytical solutions predict a case where precession occurs at two different frequencies at the two contact points. The range of whip for the contact location at the left, away from the disk, is less than the range of whip for the right location near the disk. The left contact whips at 111 Hz (close to the pitch mode of 113Hz), whereas the right contact whips at 81 Hz (close to the bounce mode of 82Hz). Beyond the whip regimes, the two contacts seem to whirl again. Since the whip ranges are different, the right contact jumps to whirl after the left contact and not simultaneously.

Analysis of individual contact points in Figure19 (b), shows the left contact farthest from the disk, tends to whirl initially. It then whips when entering the whipping mode of 81Hz until it reaches the next transition rotor speed. The contact velocity beyond this point again drops, followed by increases in contact velocity showing a jump to another whip at 111Hz. The velocity again falls and then increases though this time it’s perceived as whirling in the BP frequency graph Figure 19(a).

As shown in Figure 19(c), the contact closer to the disk is always whipping. Its velocity increases during the whirl regions drops when transitioning to whip (81 HZ) and then keeps increasing until it drops again slightly. This transition at 81Hz is perceived as transition to whirl on BP frequency graph.

For the second whirl regime, although the contact velocity is not zero, still the BP frequency increases with increasing rotor speed.

Figures 19(d) and 19(e) show the left and right contact two sided FFT's. The two FFT show the dominance of backward precessional frequency along with some sidebands during the whipping regions. These sidebands are seen in the region when the right contact is whipping but the left contact has entered the second whirling region.

Figure 19(f) is a plot for reducing rotor speed. The range of whip is smaller and equal for both the contact points. Unlike the predictions for increasing rotor speed, the range of whip under this condition is the same for both contact points. In this case, the contact away from the disk (left contact) whips at the bounce mode frequency. After some time, it jumps to whip the at pitch mode frequency. The right contact continues whipping at the pitch mode frequency until it transitions to whirl again.

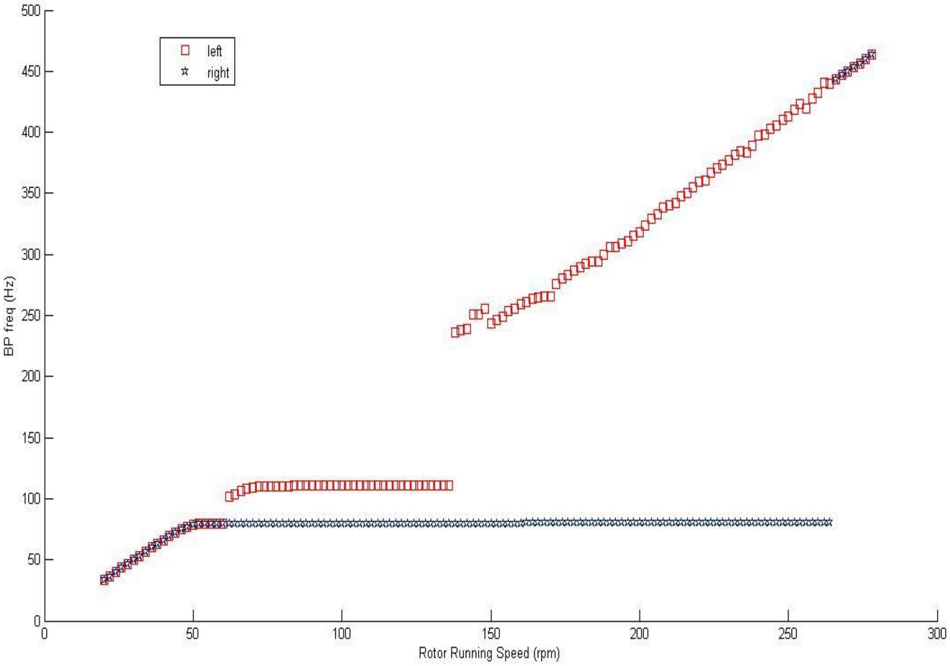

(a) Simulation Results(BP vs Increasing Rotor Speed)

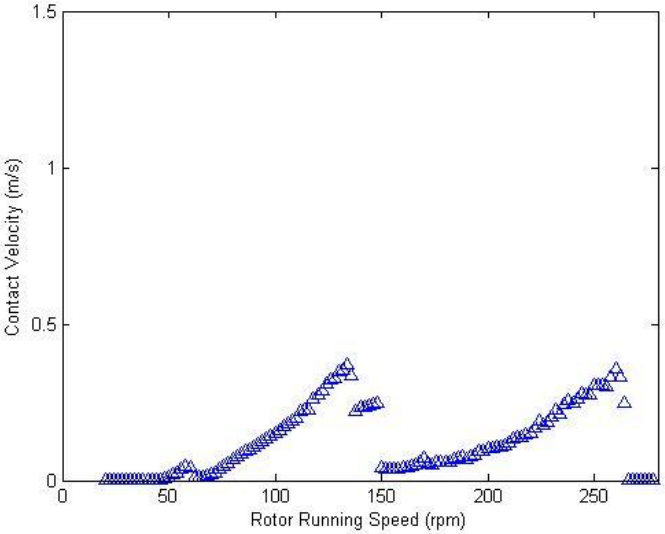

(b) Left Contact Velocity vs Rotor Speed

Figure 19 Disk at Overhang Location RCl_L= RCl_R=100.

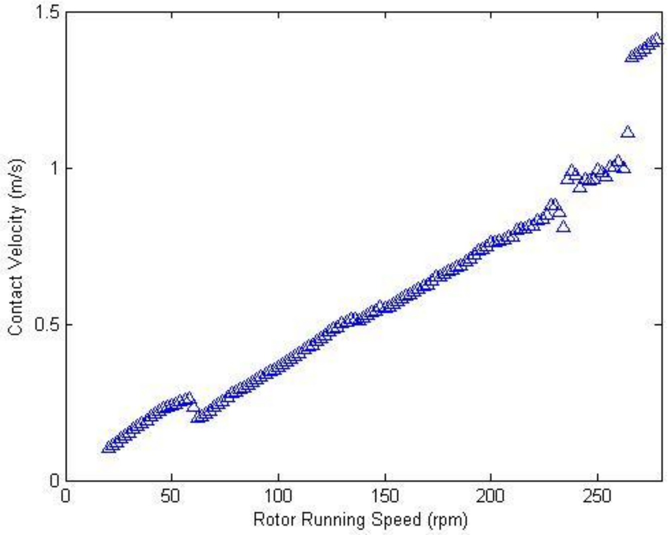

(c) Right Contact Velocity vs Rotor Speed

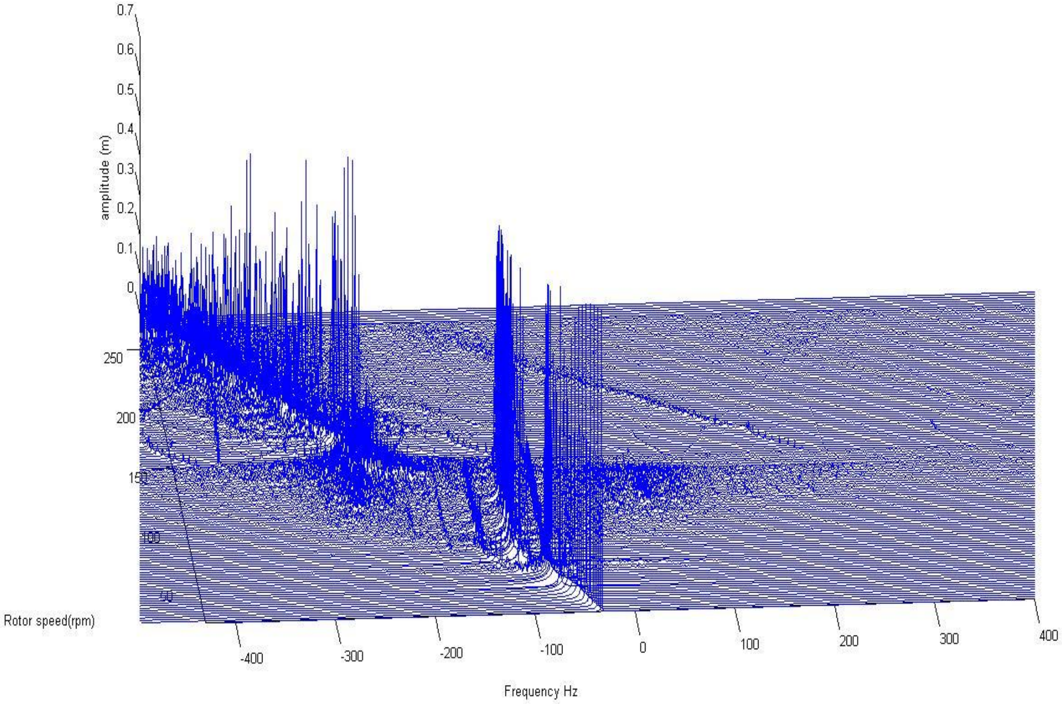

(d) Two Sided FFT, Left Contact (Increasing Rotor Speed)

Figure 19 Continued

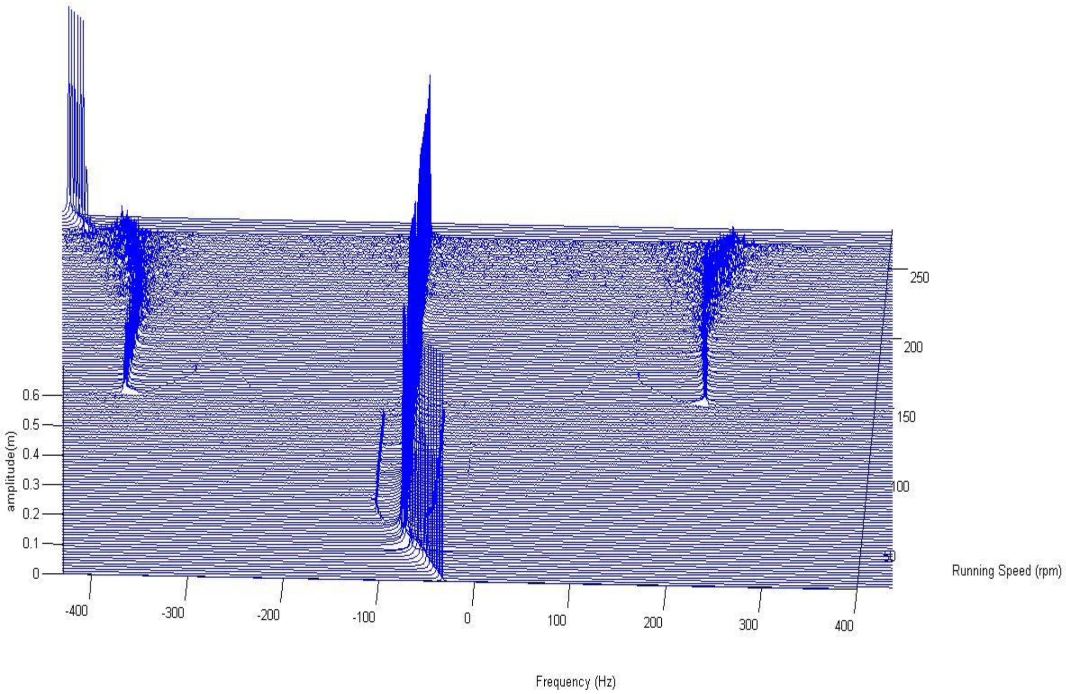

(e) Two Sided FFT, Right Contact (Increasing Rotor Speed)

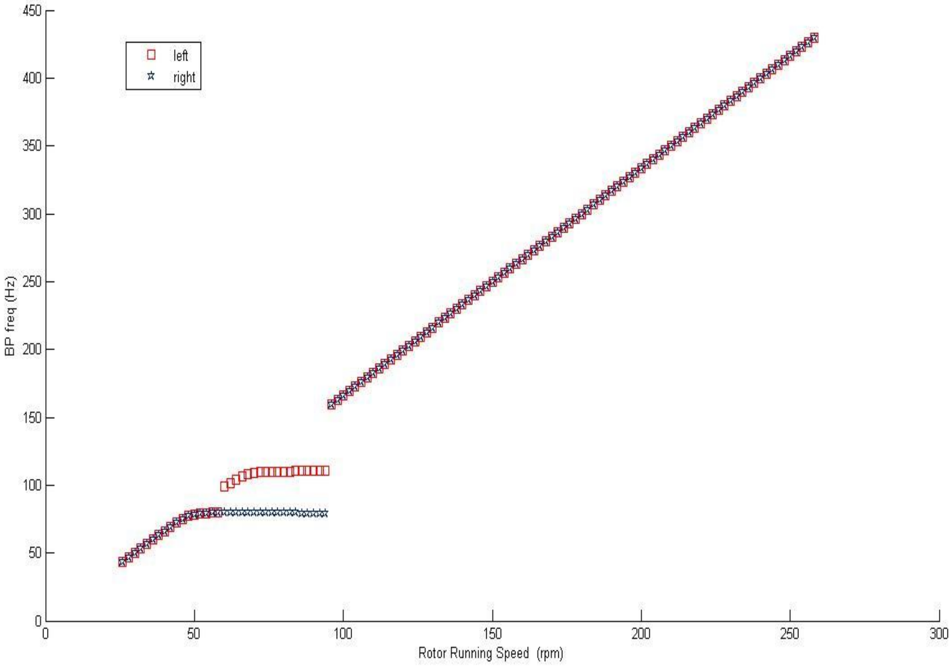

(f) Simulation Results (BP vs Decreasing Rotor Speed)

Figure 19 Continued

Subcase (b) RCl_L=100, RCl_R=125

As shown in Figure 18(a), predictions are similar to the subcase (a), Figure19 (a), except for the range of whip. The left contact RCl=100 whips at 81Hz for a longer duration as in comparison to Figure 20(a); also the range of whipping at 111 Hz has increased. On the other hand, the right contact has a reduced range of whipping as compared to the earlier case in Figure 20(a). Both contacts follow separate frequency paths when entering the second whirl region, each contact following a slope corresponding to the contact's RCl. The range of whip for the contact closer to the mass disk is larger than the other contact.

Individual investigation of contact locations confirm continuous whipping at both location in Figures 20 (b), (c). The transition from whirl to whip and vice versa on the BP plot is marked by a drop in contact velocities. As seen earlier in the case of disk at ¾ location, the contact near the disk slips more than the contact farther away. The contact with RCL=100 has a broader whip region, and the one with RCl=125 has a smaller whip region as compared to the case when both contacts have same RCl.

Figure 20(d) and Figure 20(e) are the two sided FFT's for the left and the right contacts. They show a similar trend as subcase (a) of having sidebands in the right contact whip region, for the period when the other contact has already jumped to the second whirl region. These sidebands are probably due to presence of partial rub at the surface during these rotor speeds.

Figure 20(f) is the BP frequency plot for decreasing rotor speeds. Unlike any other case, the two contacts follow different paths during the second whirling region.

Each contact point follows its own path with a slope corresponding to its RCl. Unlike the case of increasing rotor speed where jump up to the whirl region occurs at different rotor speeds, both the contacts are seen jumping down to whip at the same frequency. The left contact whips at 111Hz and right contact whips at 81 Hz. The left contact then jumps down and whips at 81 Hz, and then both the contacts enter the whirl together.

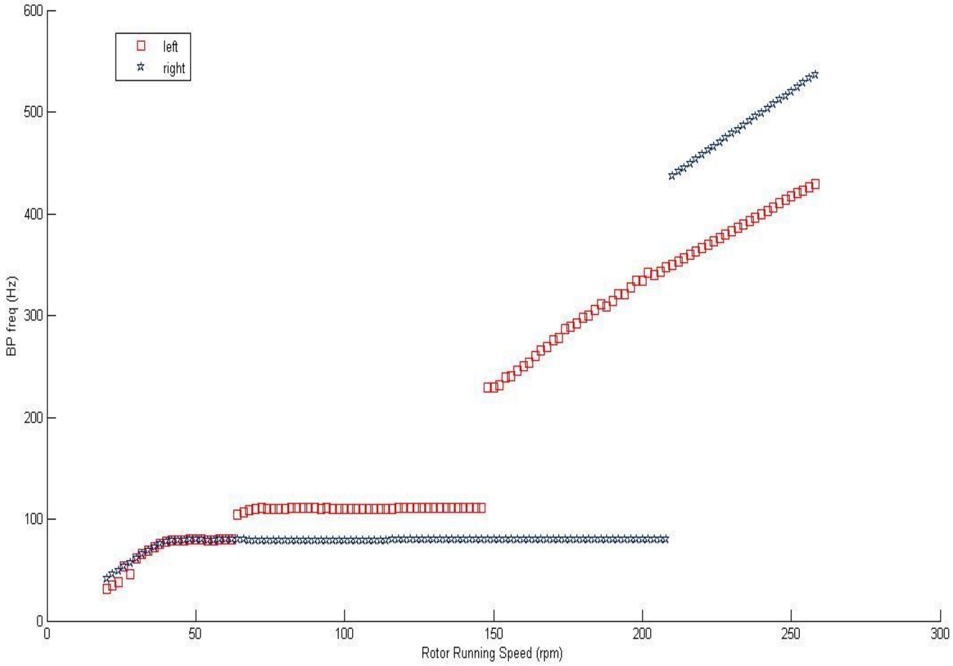

(a) Simulation Results (BP vs Increasing Rotor Speed)

Figure 20 Disk at Overhang Location RCl_L= 100, RCl_R=125

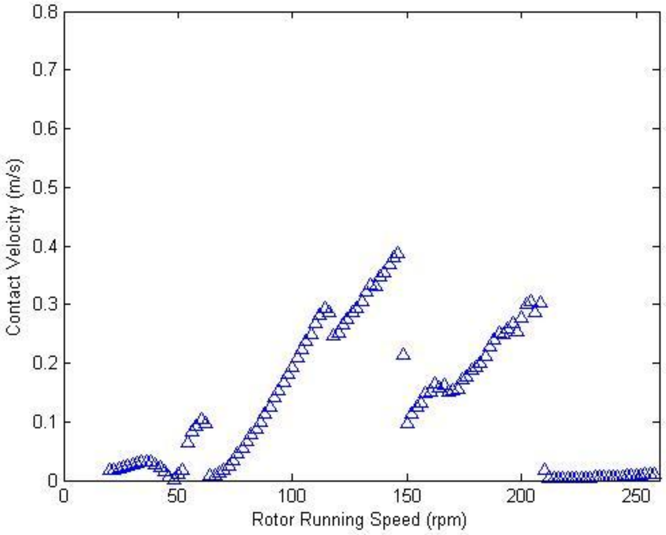

(b) Left Contact Velocity vs Rotor Speed

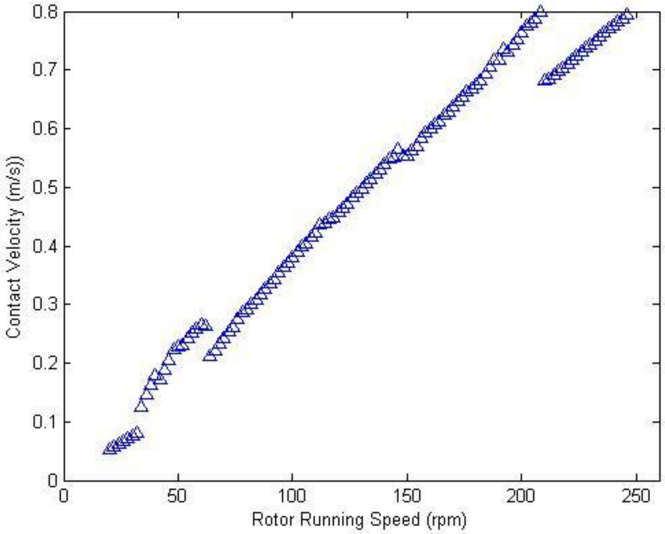

(c) Right Contact Velocity vs Rotor Speed

Figure 20 Continued

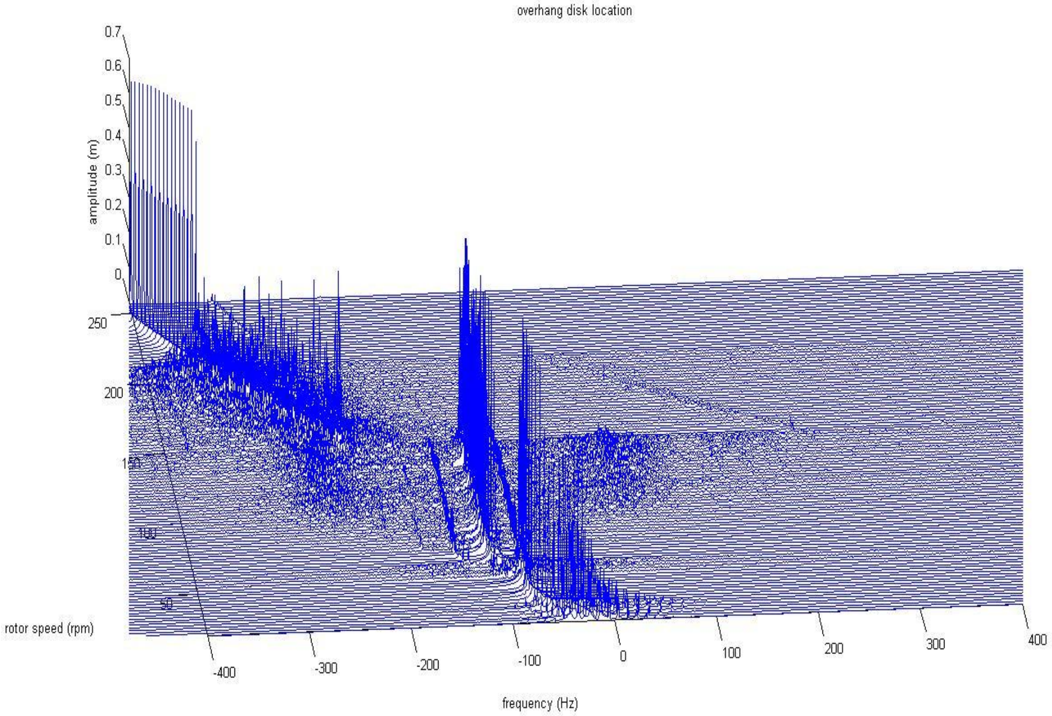

(d) Two Sided FFT, Left Contact (Increasing Rotor Speed)

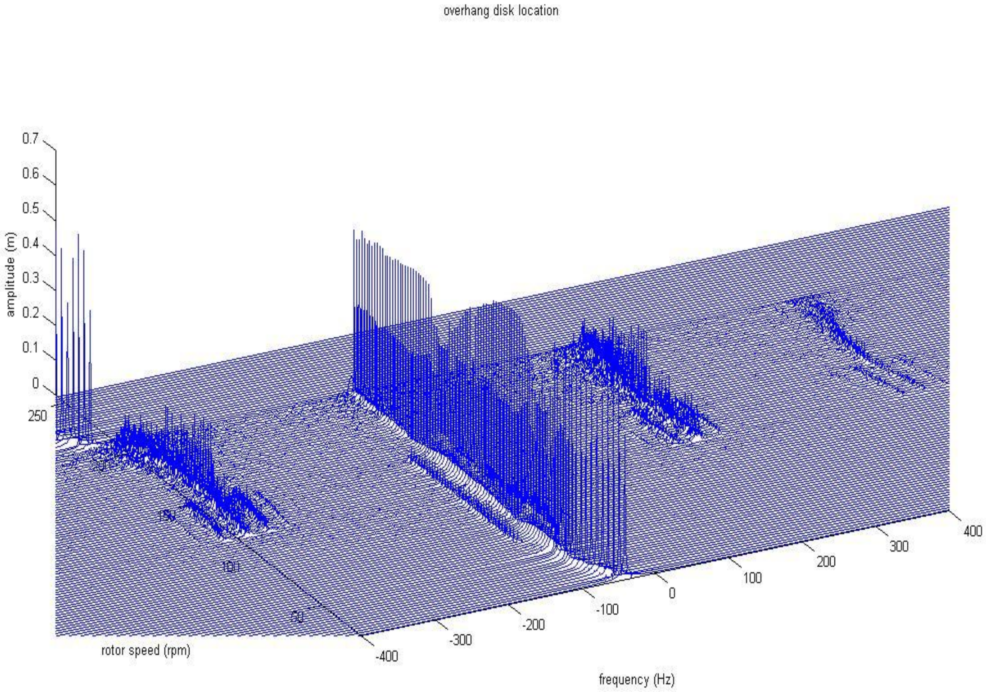

(e) Two Sided FFT, Right Contact (Increasing Rotor Speed)

Figure 20 Continued

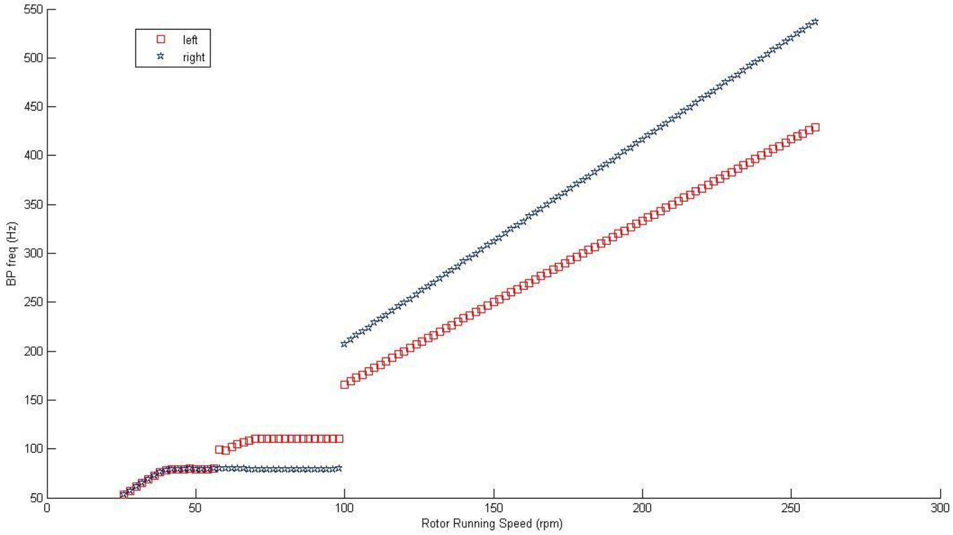

(f) Simulation Results (BP vs Decreasing Rotor Speed)

Figure 20 Continued

Subcase (c)- RCl_L=125, RCl_R=100

Looking at Figure 21(a) a similarity of prediction to subcase (a) and (b) is seen. The contact near the mass disk has a much broader whip regime. The whip further increases if this contact has RCl =100 in comparison to RCl =125 as in Figure 20, whereas the left contact whipping decreases for RCl=125 .Unlike other overhang cases, the left contact only whips at 111Hz. The right contact enters whip at 81 Hz but the left contact still whirls till it starts whipping at 111 Hz. Here, both contact locations jump to the second whirl region at different frequencies and follow the path corresponding to their respective RCl.

Individual investigation of contact location confirm whipping at both locations at all times as shown in Figure 21(b), (c). The transition from whirl to whip and vice versa on the BP plot is marked by a drop in contact velocities in this plot. Again, the contact nearer to the disk produces higher contact velocities in comparison to the velocities at the other contact. The contact with the RCl=100 has a broader whip region and the one with RCl=125 has a smaller whip region as compared to the case where both the contacts have the same RCl.

Figure 21(d), (e) are the two sided FFT plots for the left and the right contacts. They show a similar trend as subcase (a) of having sidebands in the right contact whip region, for the period when the other contact has already entered the secondary whirl region. These sidebands are probably due to partial rub at the surface during these rotor speeds.

Figure 21(f) is the BP frequency plot for decreasing rotor speeds. The two contacts follow their own path with slope corresponding to its RCl for the whirl regime. As in subcase (b) both the contacts are seen jumping down to whip at the same frequency. The left contact whips at 111Hz and the right contact whips at 81 Hz, followed by the left contact entering whirl and being joined by the right contact to whirl together.

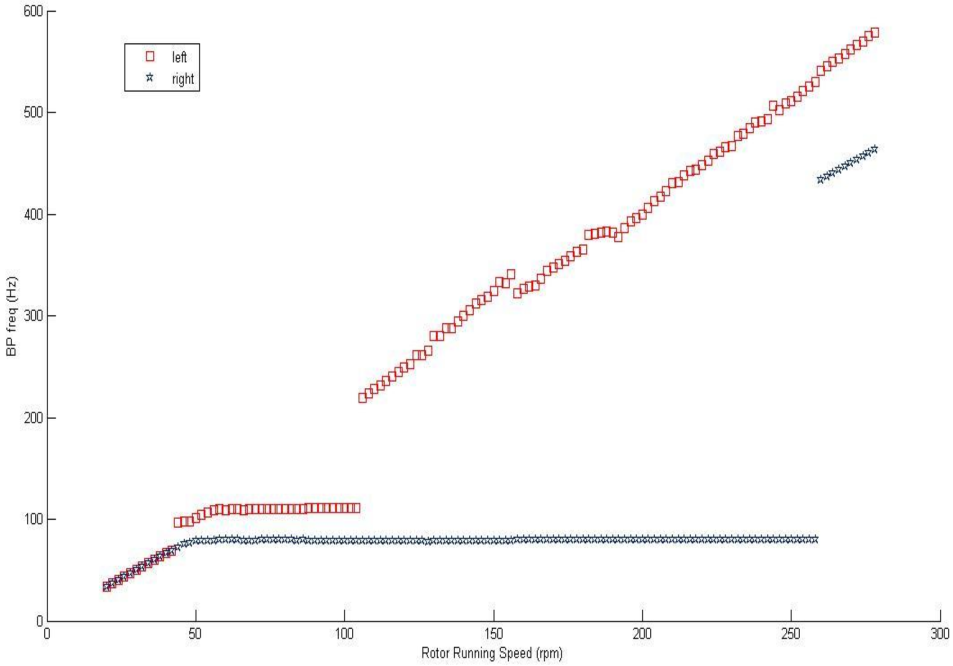

(a) Simulation Results (BP vs Increasing Rotor Speed)

Figure 21 Disk at Overhang Location RCl$_L$= 125, RCl$_R$=100

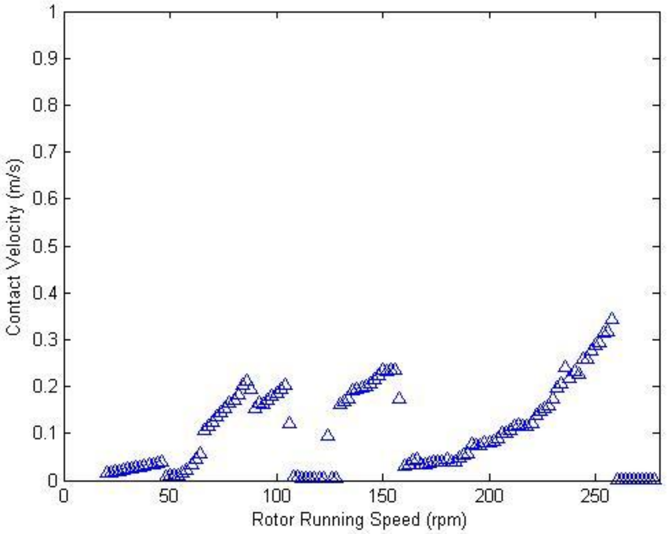

(b) Left Contact Velocity vs Rotor Speed

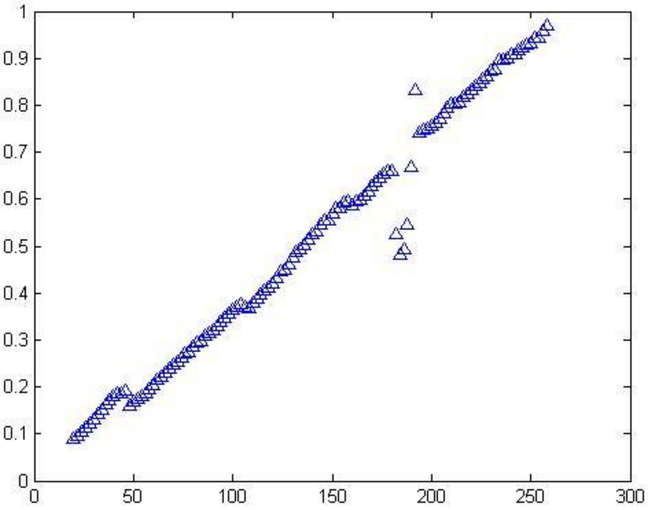

(c) Right Contact Velocity vs Rotor Speed

Figure 21 Continued

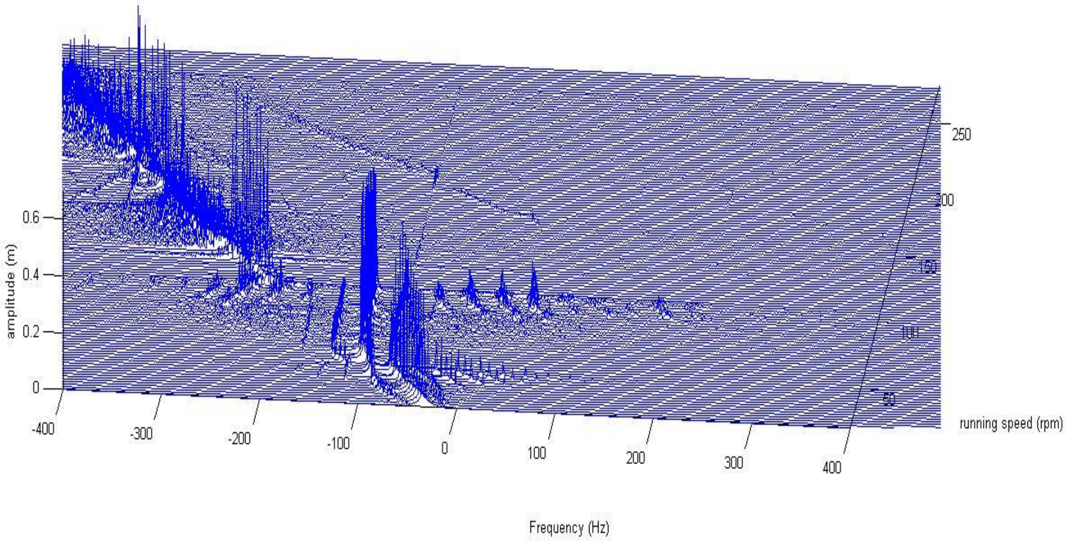

(d) Two Sided FFT, Left Contact (Increasing Rotor Speed)

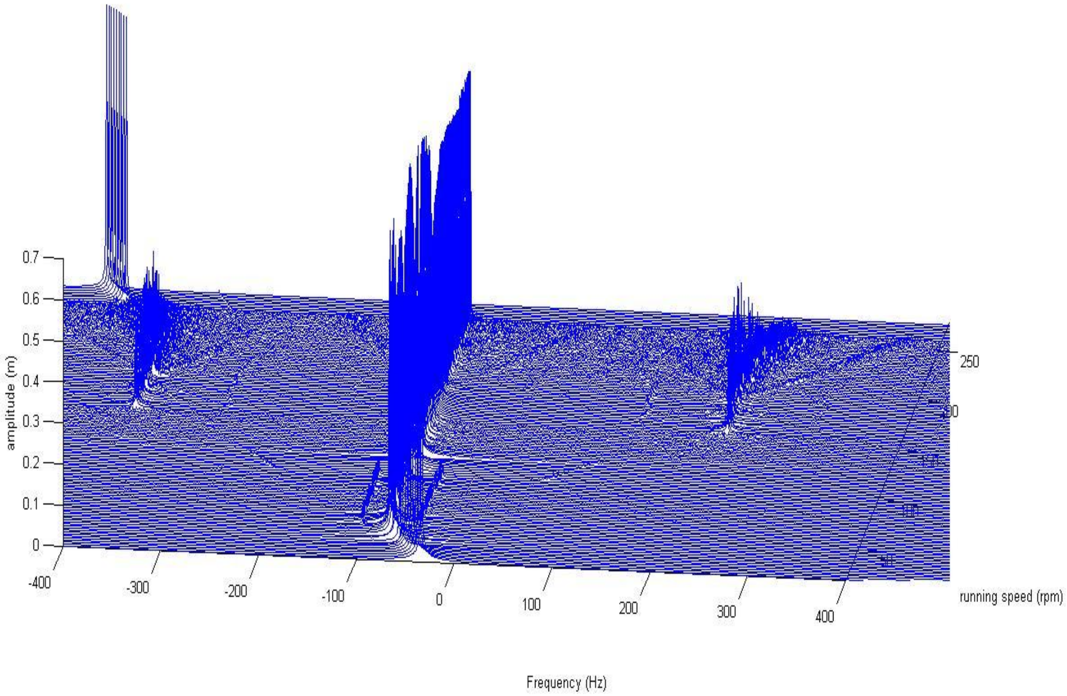

(e) Two Sided FFT, Right Contact (Increasing Rotor Speed)

Figure 21 Continued

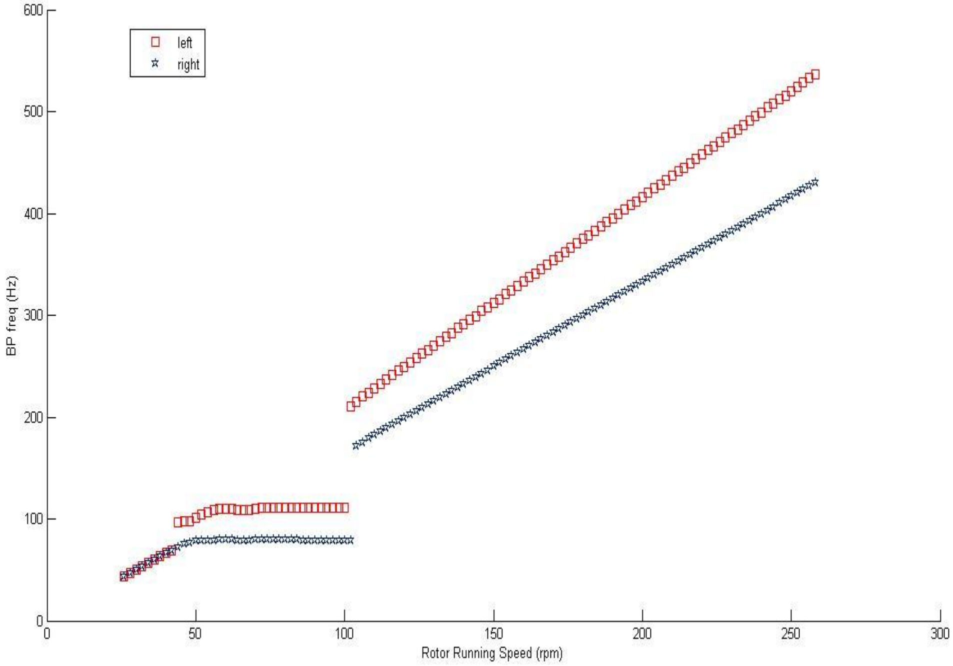

(f) Simulation Results (BP vs Decreasing Rotor Speed)

Figure 21Continued

CHAPTER V

SUMMARY AND CONCLUSION

The thesis looks at the unique characteristics related to the phenomena of dry friction whip and whirl occurring at two contact locations. An analytical model was developed for a rigid rotor with a mass disk and an elastically supported stator, with contact at two locations. Assuming that the radius to clearance (RCl) was the same at both contact location, Mode1 (normal contact forces in phase at two contacts) and Mode 2(normal contact forces out of phase at two contacts) analytical solutions were developed for three different configurations – (1) Disk at center (2) Disk at ¾ location (3) Disk at overhang location. Nonlinear time transient analyses for the flexible analog of the models were developed to validate the analytical models. Also models with different RCl at the two contacts were developed for the 3 configurations and analyzed for whirl/whip characteristics. An API imbalance is introduced for the disk at center model, but since it did not bring about a difference in predictions it wasn't used in any further models. Predictions were generated for both increasing and decreasing rotor speeds. The predictions from the two methods and conclusions drawn are summarized below.

5.1 SUMMARY MATHEMATICAL MODEL

Some characteristics of the analytical solution can be summarized are:

1) For disk at center location- Mode 1 predicts critical transition frequencies. The rotor-stator pinned frequency of 87Hz and the stator bounce frequency of 110Hz. The former is the transition from whirl to whip and the latter is the transition from whip to whirl. Since μ=.5 is chosen, 84.66Hz and 110Hz were expected points of transition since these are frequencies beyond which μ exceed 0.5

   Mode 2 predicts critical frequency of whirl to whip transition to be 130 Hz (pitch mode frequency). No other transition is predicted in the range of running speeds under observation

2) For disk at ¾ location- Like the case for disk at center, mode 1 predicts transition frequencies of whirl-to-whip and whip-to-whirl to be 87Hz and 110 Hz respectively. The transition will be expected at 82 HZ because beyond this point μ>.5. The range of whirl. after transitioning from whip is less as compared to the case of disk at center location

   Mode 2 predicts transition frequencies as 87 Hz(rotor stator bounce frequency), 98 Hz(approx stator bounce frequency), and 128Hz(pinned rotor-stator pitch frequency). Transition from whirl to whip is predicted at 87 Hz, back to whirl at 98 Hz, and then whip again at 128Hz.

3) For disk at overhang location- Mode 1 predicts certain complex characteristics for this particular configuration. A very small range of whirling is observed

common to both the contacts starting at 57Hz. This model is predicted to transition to whip at 80Hz (bounce mode frequency) and does not transition back to whirl again.

Mode 2 has a whirl-to-whip transition at 80Hz; there is no other whirl regime common to both contacts. Although a small region is seen to have a positive μ for both contacts but it does not reach the minimum μ_{req} value and hence is not seen as whirling

5.2 SUMMARY SIMULATION PREDICTION

1) Disk at center-RCl_L= RCl_R=100

   Transition from whirl to whip is predicted at 84.66 Hz. Investigation of the two contacts agree with the Backward Precession (BP) plot and predict rolling without slipping for the initial whirl, slipping along the whip region, and then rolling without slipping again for the next whirl region. Also the introduced API imbalance is not enough to bring out any change in the predictions at the speeds under observation. Decreasing speed predictions show a different whirl-to-whip jump down frequency as compared to the whip-to-whirl jump up in the speed up case. The whip range is also smaller as compared to the speed up case.

   RCl_L=100, RCl_R=125 Transition from whirl-to-whip is predicted at 84.66 Hz. Investigation of the two contacts show slipping at all conditions. The right contact slips much more than the left contact thus resulting in the BP frequency increasing with running speed. This behavior *imitates* a whirling motion on the

BP graph. Similar to the case with the same RCl, decreasing speed predictions show a different whirl-to-whip jump down frequency as compared to the whip-to-whirl jump up in the speed up case. The whip range is also smaller as compared to the speed up case.

2) Disk at ¾ location-$RCl_L= RCl_R=100$

Transition from whirl-to-whip is predicted at 82 HZ. Investigation of the velocities at the two contacts agree with the BP plot, that rolling without slipping occurs for the initial whirl, slipping along the whip region and then rolling without slipping again for the next whirl region. Decreasing speed predictions show a different whirl-to-whip jump down frequency as compared to the whip-to-whirl jump up in the speed up case. The whip range is also smaller as compared to the speed up case.

$RCl_L=100$, $RCl_R=125$ Transition from whirl to whip is predicted at 84.6 Hz, Investigation of the velocities at the two contacts show slipping at all conditions. The right contact slips much more than the left contact, resulting in the BP frequency increasing with running speed. This behavior *imitates* a whirling motion on the BP graph. Similar to the case with the same RCl, decreasing speed predictions show a different whirl-to-whip jump down frequency as compared to the whip-to-whirl jump up in the speed up case. The whip range is also smaller as compared to the speed up case.

$RCl_L=125$, $RCl_R=100$ Transition from whirl to whip is predicted at 84.6Hz, Investigation of the velocities at the two contacts show slipping at all times. The right contact slips much more than the left contact, resulting in BP frequency increasing with running speed. This behavior *imitates* a whirling motion on the BP graph. There is difference in whirl-to-whip jump down frequency as compared to speed up whip-to-whirl jump up frequency. Also the whip region is smaller for the speed down case as compared to the speed up case.

3) Disk at overhang position-RCl_L= RCl_R=100

Transition from whirl-to-whip is predicted at 81Hz. The left contact motion then jumps to whip at 111Hz. Contact near the disk has a broader range of whip as compared to the other contact. Investigation of individual contacts shows the left contact actually rolls without slipping for the initial whirl region. Slipping occurs beyond that transition, On the other hand, the right contact slips at all times. Decreasing speed predictions have a same whirl-to-whip jump down frequencies for both contacts as compared to different whip-to-whirl jump up frequencies for the two contacts in the speed up case. The whipping range is equal for both contacts as compared to different whipping ranges for the speed up case.

RCl_L=100, RCl_R=125 Transition from whirl to whip is predicted at 81Hz. The left contact then jumps to whip at 111Hz. Contact near the disk has a broader range of whip as compared to the other contact. Slipping occurs at both contacts at all times, the contact near the disk slips more than the other. The contact with the RCl=100 has a broader whip region, and the one with RCl=125 has a smaller whip region as compared to the case when both the contacts had the same RCl.

When transitioning from whip to whirl, both contacts transition at different frequencies and follow paths corresponding to the respective RCl. . Decreasing speed predictions have a same whirl-to-whip jump down frequencies for both contacts as compared to different whip-to-whirl jump up frequencies for the two contacts in the speed up case. The whipping range is equal for both contacts as compared to different whipping ranges for the speed up case.

RCl_L=125, RCl_R=100 Transition from whirl to whip is predictive at 81Hz. The left contact directly jumps to 111Hz. Contact near the disk has a broader range of whip as compared to the other contact. Slipping occurs at both contacts at all conditions; the contact near the disk slips more than the other. The contact with RCl=100 has a broader whip region, and the one with RCl=125 has a smaller whip region as compared to the case when both the contacts had same RCl. When transitioning from whip to whirl, both contacts transition different frequencies and follow paths corresponding to the respective RCl. Decreasing speed predictions have a same whirl-to-whip jump down frequencies for both contacts as compared to different whip-to-whirl jump up frequencies for the two contacts in the speed up case. The whipping range is equal for both contacts as compared to different whipping ranges for the speed up case.

5.3 CONCLUSIONS

The analytical solution predicts a very accurate first whirl-to-whip transition as validated by the simulation. This transition for the center position and ¾ position happens at 84.6 Hz and 82 Hz as is also predicted by the simulation model. As stated earlier, because of simulation limitation (simulation run for intermittent rotor speeds thus can jump to a more dominant frequency), for ¾ location it also whips at 84.6 Hz for most of the whipping region. For the overhang model, neither of the modes predict two separate whipping frequencies. The predicted transition from whip-to-whirl was not validated by the simulation predictions.

For the cases of the disk at the center and the ¾ location, the case of RCL=100 at both locations produce BP plots which predict slipping or rolling without slipping at the contact locations. The other two conditions for the two configurations imitate results of whirl and whip, both are actually slipping at all times.

Another conclusion that can be made from the simulation predictions for the disk at ¾ location and the overhang disk is that the contact which is nearer the disk slips more than the other contact.

Also for the overhang disk, the range of whip for a contact is dominated by nearness to the disk, but it is also affected by the RCl. The case with contact near to the disk with RCl=100 will whip for a greater range as compared to case with contact near the disk having RCl=125.

The whip-to-whirl jump up for speed up case is distinctively different as compared to whirl-to-whip jump down for speed down case. Also speed up case has a reasonably broader whip regime as compared to the speed down case for all the three configurations

REFERENCES

1. Rosenblum, V. I., 1995, “Entstehung mehrfacher Wellenbrüche nach dem Bruch einer Laufschaufeloder Radscheibe bei Dampfturbinen,” Allianz Report, **68**(5), pp. 176-179

2. Newkirk, B. L., 1926, “Shaft Rubbing,” Mech. Eng., **48**, pp. 830–832.

3. Baker, J. G., 1933, “Self-induced Vibration,” ASME J. Appl. Mechs., **1**, pp. 5–12.

4. Den Hartog, J. P., 1956, *Mechanical Vibrations*, 4th edition, McGraw-Hill, New York.

5. Black, H. F., 1967, “Synchronous Whirling of a Shaft Within a Radially Flexible Annulus Having Small Radial Clearance,” Proc. Inst. Mech. Eng, Paper No. 4, 181, pp. 65–73.

6. Black, H. F., 1968, “Interaction of a Whirling Rotor with a Vibrating Stator across a Clearance Annulus,” J. Mech. Eng. Sci., **10**(1), pp. 1–12.

7. Crandall, S., 1990, “From Whirl to Whip in Rotordynamics,” *IFToMM Third Intl. Conf. on Rotordynamics,* Lyon, France, pp. 19–26.

8. Lingener, A., 1990, “Experimental Investigation of Reverse Whirl of a Flexible Rotor,” *IFToMM Third Intl. Conf. on Rotordynamics,* Lyon, France, pp. 13–18.

9. Choi Y.S., 2002, “Investigation on the Whirling Motion of Full Annular Rub,” J. Sound Vib., **258**(1), pp. 191–198.

10. Bartha, A. R., 2000, “Dry Friction Backward Whirl of Rotors,” Dissertation ETH No. 13817, ETH Zurich.

11. Yu, J. J., Goldman, P., and Bently, D., 2000, “Rotor/Seal Experimental and Analytical Study of Full Annular Rub,” *Proc. of ASME IGTI Turboexpo 2000,* ASME, New York, Vol. 2000-GT-389, pp. 1–9.

12. Childs, D. W., and Bhattacharya, A., 2007, “Prediction of Dry-Friction Whirl and Whip between a Rotor and a Stator,” ASME J. Vib. Acoust., **129**, pp. 355–362.

13. Dyck, B.J., 2007, “Experimental Study of Dry-Friction Whirl and Whip for a Rotor Supported by an Annular Rub Surface,” Nothrop Grumman Space Technology Project Report, Texas A&M University, College Station, TX.

14. Wilkes, J.C., Dyck, B. J., Childs, D. W., Phillips, S. G., 2009, "The Numerical and Experimental Characteristics of Multi-Mode Dry-Friction Whip and Whirl," *GT2009-59459, ASME International Gas Turbine Institute 2009,* Orlando, FL, pp 8-17

15. Clark, S.H., Clay, H., Goglia, J.A., Hoopes, T.R., Jacobs, Smith, R.P., 2009, "Investigation of the NRG #40 Anemometer Slowdown," *American Wind Energy Association, Windpower 2009***,** Chicago, IL, pp. 1-16.

16. Childs, D.W., 2009, "Dry-friction Whirl and Whip for Contact at Two Locations," Personal communication, Texas A&M University , College Station, TX.

17. Kärkkäinen, A., Helfert, M., Aeschlimann, B., Mikkola A., 2008 "Dynamic Analysis of Rotor System With Misaligned Retainer Bearings," ASME J. Tribol. **130,** 021102

18. Hunt, K. H., and Crossley, F. R., 1975, "Coefficient of Restitution Interpreted as Damping in Vibroimpact," ASME J. Appl. Mech., **42**, pp. 440.

19. Nelson, H.D., 1980, " A Finite Shaft Element Using Timoshenko Bean Theory," ASME J. Mech, Eng. **102**(4), pp 793-431.

20. Childs, D.W., 1993, *Turbomachinery Rotordynamics: Phenomena, Modeling, and Analysis,* John Wiley and Sons, New York, pp. 395-431, Chap7.

21. TAMU Turbomachinery Laboratory, 2002,"XLTRC^2 Brochure," Texas A&M University, College Station, TX.

22. Wilkes, J.C., 2007 "A Perspective on the Numerical and Experimental Characteristics of Multi-mode Dry-friction Whip and Whirl," M.S. Thesis, Texas A&M, College Station, TX.

VITA

Name: Dhruv Dileep Kumar

Address: Department of Mechanical Engineering
c/o Dr. Dara Childs
Texas A&M University
College station, TX 77840

Email Address: logic87@mail.com

Education: B.Tech., Mechanical Engineering, NIT Kurukshetra, 2008
M.S., Mechanical Engineering, Texas A&M University, 2010